

Linear stability of slip pipe flow

Kaiwen Chen, Baofang Song [†]

Center for Applied Mathematics, Tianjin University, Tianjin 300072, China

(Received 1 February 2022)

We investigated the linear stability of pipe flow with anisotropic slip length at the wall by considering streamwise and azimuthal slip separately as the limiting cases. Our numerical analysis shows that streamwise slip renders the flow less stable but does not cause instability. The exponential decay rate of the least stable mode appears to be $\propto Re^{-1}$ when the Reynolds number is sufficiently large. Azimuthal slip can cause linear instability if the slip length is sufficiently large. The critical Reynolds number can be reduced to a few hundred given large slip lengths. Besides numerical calculations, we present a mathematical proof of the linear stability of the flow to three-dimensional yet streamwise-independent disturbances for arbitrary Reynolds number and slip length, as an alternative to the usual energy analysis. Meanwhile we derived analytical solutions to the eigenvalue and eigenvector, and explained the structure of the spectrum and the dependence of the leading eigenvalue on the slip length. The scaling of the exponential decay rate of streamwise independent modes is shown to be rigorously $\propto Re^{-1}$. Our non-modal analysis shows that overall streamwise slip reduces the non-modal growth and azimuthal slip has the opposite effect. Nevertheless, both slip cases still give the Re^2 -scaling of the maximum non-modal growth and the most amplified disturbances are still streamwise rolls, which are qualitatively the same as in the no-slip case.

Key words:

1. Introduction

The classic pipe flow with no-slip boundary condition has been proved linearly stable to axisymmetric perturbations (Herron 1991, 2017), and numerical studies suggest that the flow is linearly stable to any perturbations at arbitrary Reynolds numbers (Meseguer & Trefethen 2003). The recent work of Chen *et al.* (2019) presented a rigorous proof of the linear stability of the flow to general perturbations at high Reynolds number regime. Therefore, transition to turbulence in pipe flow is subcritical via finite-amplitude perturbations (see e.g. Eckhardt *et al.* (2007); Avila *et al.* (2011)).

However, velocity slip of viscous fluid can occur on super-hydrophobic surfaces (Voronov *et al.* 2008; Rothstein 2010), for which slip boundary condition instead of the classic no-slip condition should be adopted for the momentum equations, and the slip boundary condition can potentially influence the stability of the flow. A simplified and widely used slip boundary condition is the Navier slip boundary condition, which has been shown to apply to many flow problems and frequently adopted for linear stability studies (Vinoogradova 1999; Lauga & Cossu 2005; Min & Kim 2005; Gan & Wu 2006; Ren *et al.* 2008; Ghosh *et al.* 2014; Seo & Mani 2016; Chattopadhyay *et al.* 2017, to list a few). For pipe geometry, although many studies have investigated the linear stability of immiscible and

[†] Email address for correspondence: baofang_song@tju.edu.cn

miscible multi-fluid flows with either no-slip or Navier slip boundary condition (Hu & Joseph 1989; Joseph 1997; Li & Renardy 1999; Selvam *et al.* 2007; Sahu 2016; Chattopadhyay *et al.* 2017, etc.), much fewer studies were dedicated to the linear stability of single-phase pipe flow with slip boundary condition. Průša (2009) investigated this problem and showed that, subject to Navier slip boundary condition, pipe flow becomes less stable compared to the no-slip case, however, the destabilization effect is constrained to small Reynolds numbers and is not sufficient to render the flow linearly unstable. Their results indicated that the stability property of pipe flow is not qualitatively affected by the slip boundary condition, regardless of the slip length. For its counterpart in plane geometry, i.e. channel flow, on the contrary, Min & Kim (2005); Lauga & Cossu (2005) reported a stabilizing effect of velocity slip on the linear stability.

Usually, slip length is assumed homogeneous and isotropic, i.e. independent of position and direction at the wall in stability analysis. However, anisotropy in the effective slip length can be incurred by anisotropy in the texture pattern on superhydrophobic surfaces, such as parallel periodic slats, grooves and grates (Lecoq *et al.* 2004; Bazant & Vinogradova 2008; Ng & Wang 2009; Belyaev & Vinogradova 2010; Asmolov & Vinogradova 2012; Pralits *et al.* 2017). For example, Ng & Wang (2009) reported a ratio of down to about 0.25 between the transverse slip length (in the direction perpendicular to the slats) and longitudinal slip length (parallel to the slats). The linear stability of channel flow with anisotropic slip caused by parallel micro-graves was analyzed by Pralits *et al.* (2017) using the tensorial formulation of slip boundary condition proposed by Bazant & Vinogradova (2008). Their results showed possibilities of linear instability using special alignment of the micro-graves. Recently, Chai & Song (2019) studied the linear stability of single-phase channel flow subject to anisotropy in slip length by considering streamwise and azimuthal slip separately as the limiting cases, which can potentially be realized or approximated by using specially designed surface texture, e.g. specially aligned micro-grates/graves, according to Bazant & Vinogradova (2008). Their results showed that streamwise slip mainly stabilizes the flow (with increased critical Reynolds number), although it surprisingly destabilizes the flow slightly in a small Reynolds number range, and that azimuthal slip can greatly destabilize the flow and reduce the critical Reynolds number given sufficiently large slip length. The critical Reynolds number can be reduced to a few hundred with a dimensionless azimuthal slip length of $\mathcal{O}(0.1)$, in contrast to $Re_{cr} = 5772$ for the no-slip case. Their study also indicated that Squire's theorem (Squire 1933) ceases to apply when the wall normal velocity and vorticity are coupled via the slip boundary condition, such that the leading instability becomes three dimensional (3-D) rather than two dimensional (2-D) when slip length is sufficiently large, in agreement with Pralits *et al.* (2017). The stability of 3-D perturbations was not considered by Min & Kim (2005); Lauga & Cossu (2005) in which Squire's theorem was seemingly assumed.

Differing from channel flow, linear instability is absent at arbitrary Reynolds numbers in classic pipe flow. This raises the question of whether the anisotropy in slip length can also cause linear instability in pipe flow. To our knowledge, this problem has not been studied in pipe geometry. The pseudospectrum analysis of classic pipe flow of Schmid & Henningson (1994); Meseguer & Trefethen (2003) suggests that, despite the linear stability, at sufficiently large Reynolds numbers, a small perturbation to the linear operator associated with the governing equation can possibly change the stability of the system. The slip boundary condition can be thought of as a perturbation to the linear operator with no-slip boundary condition. However, Průša (2009) showed that homogeneous and isotropic slip does not change the spectrum qualitatively no matter how large the slip length (i.e. operator perturbation) is. Following Chai & Song (2019), in this work, we

still consider anisotropic slip length in the limiting cases and explore the possibility of linear instability for pipe flow. Aside from the critical Reynolds number as focused on by Chai & Song (2019), here we also investigate the effects of the slip on the spectrum and on the scaling of the leading eigenvalues with Reynolds number. Besides numerical calculations, we also perform analytical studies on the eigenvalues and eigenvectors of the 3-D yet streamwise-independent modes, and discuss about their structure as well as their dependence on the slip length on a theoretical basis, which to our knowledge have not been reported in the literature.

2. Numerical methods

The nondimensional incompressible Navier-Stokes equations read

$$\frac{\partial \mathbf{u}}{\partial t} + \mathbf{u} \cdot \nabla \mathbf{u} = -\nabla p + \frac{1}{Re} \nabla^2 \mathbf{u}, \quad \nabla \cdot \mathbf{u} = 0, \quad (2.1)$$

where \mathbf{u} denotes velocity and p denotes pressure. For pipe geometry, cylindrical coordinates (r, θ, x) are considered, where r , θ and x denote the radial, azimuthal, and streamwise coordinates, respectively. Velocity components u_r , u_θ and u_x are normalized by $2U_b$ where U_b is the bulk speed (the average of the streamwise velocity on the pipe cross-section), length by pipe radius R and time by R/U_b . The Reynolds number is defined as $Re = U_b R / \nu$ where ν is the kinematic viscosity of the fluid. In order to eliminate the pressure and impose the incompressibility condition, we adopt the velocity-vorticity formulation of Schmid & Henningson (1994), with which the governing equations of disturbances reduce to only two equations about the wall normal velocity u_r and wall normal vorticity η . With a Fourier-Fourier-Chebyshev collocation discretization, considering perturbations of the form of $\{u_r, \eta\} = \{\hat{u}_r(r), \hat{\eta}(r)\} e^{-i(\alpha x + n\theta)}$, the governing equations in the Fourier spectral space read

$$L\mathbf{q} + \frac{\partial}{\partial \tau} M\mathbf{q} = 0, \quad (2.2)$$

where

$$L = \begin{pmatrix} i\alpha Re U \Gamma + i \frac{\alpha Re}{r} \left(\frac{U'}{k^2 r} \right)' + \Gamma(k^2 r^2 \Gamma) & 2\alpha n^2 Re \Gamma \\ -\frac{iU'}{r} + \frac{2\alpha}{Re} \Gamma & i\alpha Re k^2 r^2 U + \phi \end{pmatrix}, \quad (2.3)$$

$$M = \begin{pmatrix} \Gamma & 0 \\ 0 & k^2 r^2 \end{pmatrix}, \quad (2.4)$$

$\tau = \frac{t}{Re}$ is the scaled time, and unknowns are

$$\mathbf{q} = \begin{pmatrix} \hat{\Phi} \\ \hat{\Omega} \end{pmatrix} = \begin{pmatrix} -ir\hat{u}_r \\ \frac{\alpha r\hat{u}_\theta - n\hat{u}_x}{nRek^2 r^2} \end{pmatrix} = \begin{pmatrix} -ir\hat{u}_r \\ \hat{\eta} \\ inRek^2 r \end{pmatrix}. \quad (2.5)$$

The real number α is the axial wave number and n , which is an integer, is the azimuthal wavenumber. The base flow is denoted as U , $k^2 = \alpha^2 + \frac{n^2}{r^2}$, $i = \sqrt{-1}$ and the prime denotes the derivative with respect to r . The operators Γ and ϕ are defined as $\Gamma = \frac{1}{r^2} - \frac{1}{r} \frac{d}{dr} \left(\frac{1}{k^2 r} \frac{d}{dr} \right)$ and $\phi = k^4 r^2 - \frac{1}{r} \frac{d}{dr} \left(k^2 r^3 \frac{d}{dr} \right)$. The other two velocity components

\hat{u}_x and \hat{u}_θ can be calculated as

$$\hat{u}_x = -\frac{\alpha}{k^2 r} \frac{\partial \hat{\Phi}}{\partial r} - n^2 r \hat{\Omega}, \quad \hat{u}_\theta = -\frac{n}{k^2 r^2} \frac{\partial \hat{\Phi}}{\partial r} + \alpha n r Re \hat{\Omega}. \quad (2.6)$$

We use the Robin-type Navier slip boundary condition at the pipe wall for streamwise and azimuthal velocities separately, i.e.

$$\left(l_x \frac{\partial u_x}{\partial r} + u_x \right) \Big|_{r=1} = 0, \quad \left(l_\theta \frac{\partial u_\theta}{\partial r} + u_\theta \right) \Big|_{r=1} = 0, \quad (2.7)$$

where $l_x \geq 0$ and $l_\theta \geq 0$ are streamwise and azimuthal slip lengths, respectively, and are independent of each other. In spectral space, these boundary conditions apply identically to \hat{u}_x and \hat{u}_θ given the homogeneity of the slip length. We use the no-penetration condition for the wall-normal velocity component at the wall, i.e. $u_r(1, \theta, x, t) = 0$. Lauga & Cossu (2005); Chai & Song (2019) considered the same boundary conditions for slip channel flow. Note that in the isotropic slip case considered by Průša (2009), l_x and l_θ are related as $l_\theta = \frac{l_x}{1 + l_x}$, which gives $l_\theta \approx l_x$ for small slip lengths. With boundary condition (2.7), given that we impose the same volume flux as in the no-slip case, i.e.

$$\int_0^1 U_x(r) r dr = \frac{1}{4}, \quad (2.8)$$

the velocity profile of the constant-volume-flux base flow reads

$$\mathbf{U}(r) = \frac{1 - r^2 + 2l_x}{1 + 4l_x} \hat{\mathbf{x}}, \quad (2.9)$$

where $\hat{\mathbf{x}}$ represents the unit vector in the streamwise direction. Note that the base flow is independent of l_θ . Converting to the $(\hat{\Omega}, \hat{\Phi})$ system, the boundary condition (2.7) reads

$$\frac{\alpha}{k^2} \frac{\partial \hat{\Phi}}{\partial r} + n^2 Re \hat{\Omega} + l_x \left(n^2 Re \frac{\partial \hat{\Omega}}{\partial r} + \frac{\alpha}{k^2} \frac{\partial^2 \hat{\Phi}}{\partial r^2} + \alpha \frac{n^2 - \alpha^2}{(n^2 + \alpha^2)^2} \frac{\partial \hat{\Phi}}{\partial r} \right) = 0 \quad (2.10)$$

and

$$\alpha n Re \hat{\Omega} - \frac{n}{n^2 + \alpha^2} \frac{\partial \hat{\Phi}}{\partial r} + l_\theta \left(\alpha n Re \hat{\Omega} + \alpha n Re \frac{\partial \hat{\Omega}}{\partial r} - \frac{n}{n^2 + \alpha^2} \frac{\partial^2 \hat{\Phi}}{\partial r^2} + \frac{2n\alpha^2}{(n^2 + \alpha^2)^2} \frac{\partial \hat{\Phi}}{\partial r} \right) = 0. \quad (2.11)$$

It can be seen that $\hat{\Omega}$ and $\hat{\Phi}$, i.e. \hat{u}_r and $\hat{\eta}$, are coupled via the slip boundary condition.

In order to avoid the singularity at the pipe center, i.e. $r = 0$, the domain $[0, 1]$ is extended to $[-1, 1]$ and an even number of Chebyshev grid points over $[-1, 1]$ are used such that there is no grid point at $r = 0$. This extension also allows us to use the Chebyshev collocation method for the discretization in the radial direction and the resulted redundancy is circumvented by setting proper parity conditions on $\hat{\Phi}$ and $\hat{\Omega}$ with respect to r (Trefethen 2000; Meseguer & Trefethen 2003). In this way, no explicit boundary condition is imposed at the pipe center.

To determine whether a mode (α, n) is linearly stable or not, one only needs to calculate the eigenvalues of the operator $-M^{-1}L$ and check if any eigenvalue has a positive real part, λ_r , which determines the asymptotic growth/decay rate of the corresponding eigenvector as $t \rightarrow \infty$.

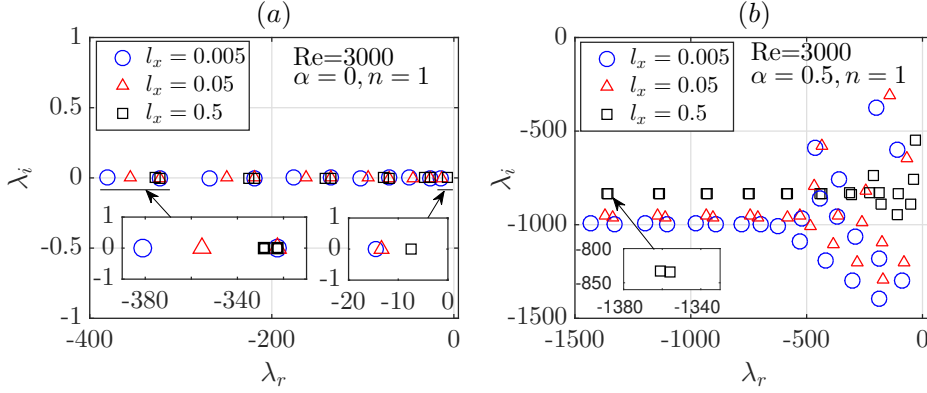


FIGURE 1. Spectrum of the flow at $Re = 3000$ with $l_x = 0.005$ (circles), 0.05 (triangles) and 0.5 (squares). (a) The mode $(\alpha, n) = (0, 1)$. (b) The mode $(\alpha, n) = (0.5, 1)$.

3. Streamwise slip

We consider the case of $l_x \neq 0$ and $l_\theta = 0$ as the limiting case of streamwise slip being significant and azimuthal slip being negligible.

The effect of the slip on the spectrum is investigated for $Re = 3000$ and is shown in Figure 1 for the modes $(\alpha, n) = (0, 1)$ and $(0.5, 1)$. Firstly, panel (a) shows that the eigenvalues of the $(\alpha, n) = (0, 1)$ mode visually all fall on the $\lambda_i = 0$ line (λ_i denotes the imaginary part of the eigenvalue) and in the left half-plane, which suggests that the eigenvalues are all real and negative. Meseguer & Trefethen (2003) reported the same finding for the no-slip case in a large Reynolds number range up to 10^7 . In fact, the eigenvalues being real and negative can be rigorously proved, see our proof in Section 5.1. Secondly, as l_x increases, it can be observed that there are two groups of eigenvalue, one of which stays constant and the other of which shifts to the right, see the two insets in panel (a). Specifically, as l_x is increased to 0.5 , the left eigenvalue in the left inset has moved from the circle to the triangle and finally to the square while the right eigenvalue stays constant. Nonetheless, the rightmost eigenvalue increases as l_x increases (see the right inset) which indicates that the flow becomes less stable. In Section 5.2, we will show that the former group corresponds to disturbances with $\Phi \neq 0$, i.e. $u_r \neq 0$ and the latter group, on the contrary, is associated with disturbances with $\Phi \equiv 0$, i.e. $u_r \equiv 0$ and, the rightmost eigenvalue belongs to the latter group (see Figure 13). Panel (b) shows the case for the mode $(\alpha, n) = (0.5, 1)$. The slip does not qualitatively change the shape of the spectrum. As l_x increases, the eigenvalues overall move to the right. Besides a horizontal shift, there is a shift in the vertical direction either, and meanwhile the spectrum is compressed in the vertical direction, see the comparison between the $l_x = 0.5$ and the other two cases. Using the term of Schmid & Henningson (1994); Meseguer & Trefethen (2003), the horizontal branch of the spectrum (the part with $\lambda_r \lesssim -600$) corresponds to mean modes, the upper branch corresponds to wall modes and the lower branch to center modes. Note that the speed of a wave is given by $\frac{-\lambda_i}{\alpha Re}$ in our formulation. It has been known that the wave speed of the mean modes follows the mean velocity of the ‘two-dimensional’ axial base flow, i.e. $\int_0^1 U_x(r) dr$ in pipe flow (see e.g. Drazin & Reid (1981)), which gives $\frac{2}{3}$ in the no-slip case (Schmid & Henningson 1994). In our case, the wave speed of the mean modes is decreased by the slip, reducing to 0.5559 for $l_x = 0.5$ ($\frac{833.868}{0.5 \times 3000}$, see the eigenvalue in Table 1) which is very close to $\frac{5}{9}$ given by $\int_0^1 U_x(r) dr$ with the base flow shown in (2.9). The wall modes, which are located close to the wall,

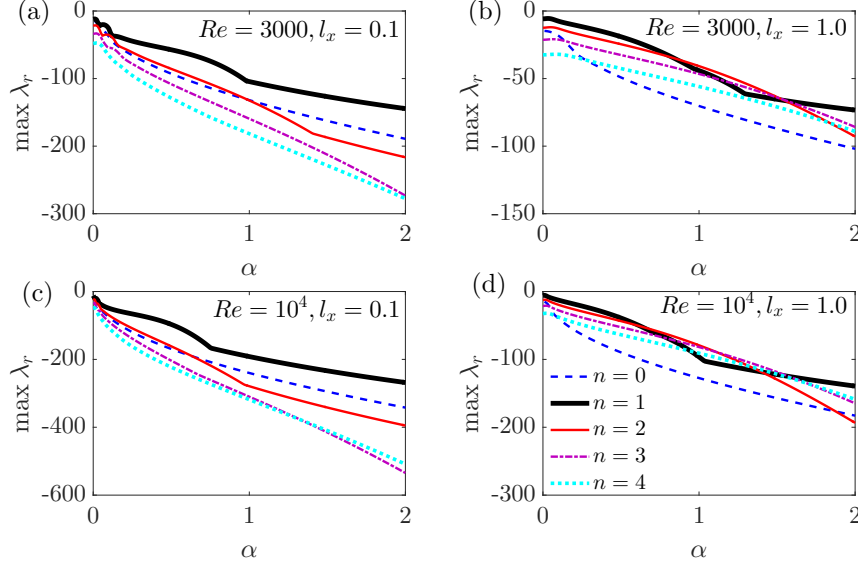


FIGURE 2. The maximum eigenvalue, $\max \lambda_r$, as a function of α , for $Re = 3000$ (a,b) and 10^4 (c,d). For each Reynolds number, azimuthal wavenumbers $n = 0, 1, 2, 3, 4$ and slip lengths $l_x = 0.1$ and 1.0 are shown.

move at lower speed than the center modes, which are located close to the pipe center and move at speeds close to the centerline velocity. Since we fix the volume flux of the flow while the slip length is varied, the speed of the base flow close to the wall increases as l_x increases, whereas the speed near the pipe center decreases, i.e. the velocity profile becomes flatter, see the base flow given by (2.9). Therefore, it can be expected that as l_x increases, the speed of the wall-modes increases and that of the center modes decreases, and all three types of modes move at closer speeds. This is exactly what the compression in the vertical direction of the spectrum reveals. The other noticeable effect is that the slip brings the adjacent eigenvalues associated with the mean modes closer as the slip length increases, causing a seemingly degeneracy of the spectrum, see Figure 1(b).

Figure 2 shows the maximum of the real part of the eigenvalue, $\max \lambda_r$, as a function of the streamwise wavenumber, α , for $Re = 3000$ and 10^4 . For each Re , slip lengths $l_x = 0.1$ and 1.0 , and azimuthal wavenumbers $n = 0, 1, 2, 3$ and 4 are considered. The trend shown in the figure suggests that, for both Reynolds numbers, $\alpha = 0$ is nearly the least stable mode, i.e. the slowest decaying mode given that all $\max \lambda_r$'s are negative, regardless of the slip length. At small α , where $\max \lambda_r$ is largest, the results suggest that $n = 1$ is always the least stable one. At larger α , however, $n = 1$ is still the least stable when l_x is small, see the case of $l_x = 0.1$ in panel (a, c), but is not in a range of α around $\alpha = 1$, see the case of $l_x = 1.0$ in panel (b, d). Nevertheless, in this range, $\max \lambda_r$ is much smaller than that in the small α regime. Therefore, as we are most interested in the least stable mode, in the following, we will focus on the $n = 1$ modes. In fact, for the $\alpha = 0$ modes, we can rigorously prove that $n = 1$ is the least stable azimuthal wavenumber, see Appendix B.

Figure 3 shows $\max \lambda_r$ as a function of α of the $n = 1$ modes for $Re = 3000$ (a) and 10^4 (b). For each Re , overall $\max \lambda_r$ increases as l_x increases, i.e. the $n = 1$ modes decay more slowly as l_x increases. The insets show the close-up of the small α region, in which the dependence of $\max \lambda_r$ on α is not monotonic, with the maximum appears at some

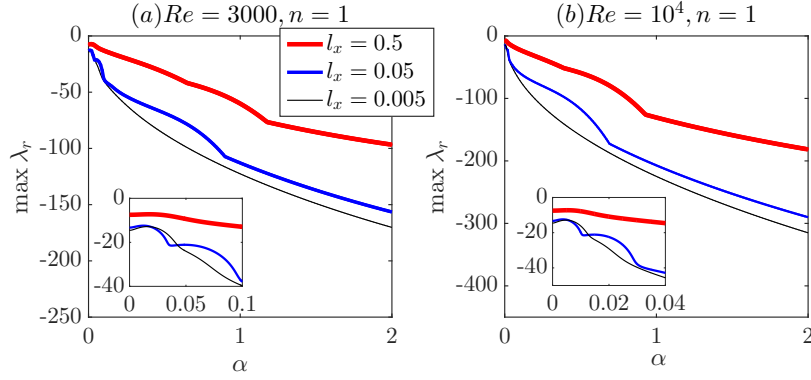


FIGURE 3. The influence of streamwise slip on $\max \lambda_r$ of $n = 1$ modes for $Re = 3000$ (a) and 10^4 (b). Slip lengths of $l_x = 0.005$ (thin black), 0.05 (blue) and 0.5 (bold red) are shown. The insets show the close-up of the regions with very small α .

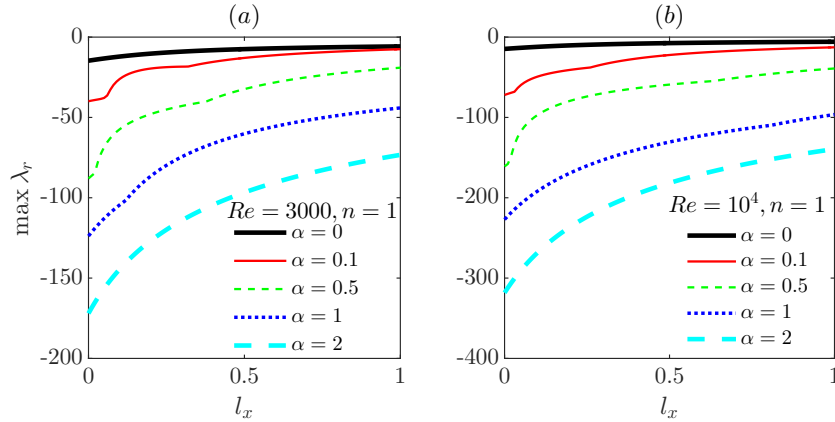


FIGURE 4. $\max \lambda_r$ of $n = 1$ modes with $\alpha = 0, 0.1, 0.5, 1.0$ and 2.0 as a function of l_x for $Re = 3000$ (a) and $Re = 10^4$ (b).

small but finite α instead of $\alpha = 0$. Nevertheless, the difference between the peak value and the value for $\alpha = 0$ is very small, i.e. $\alpha = 0$ is nearly the least stable mode, as aforementioned. In fact, the dependence on l_x is not fully monotonic either, see the very small region around $\alpha = 0.03$ for the $l_x = 0.005$ (the thin black line) and $l_x = 0.05$ (the blue line) cases as shown in the inset in (a) and around $\alpha = 0.01$ in the inset in (b). However, for $\alpha = 0$ and in most range of α , our results show a monotonic increase of $\max \lambda_r$ as l_x increases.

Figure 4 illustrates the dependence of $\max \lambda_r$ of the $n = 1$ modes on l_x in a broader range of l_x . For each Re , $\alpha = 0, 0.1, 0.5, 1$ and 2 are shown. The trend shows that as l_x keeps increasing, $\max \lambda_r$ seems to asymptotically approach a plateau with a negative value, i.e. all the modes shown in the figure appear to be linearly stable, for both Reynolds numbers.

The above results suggest that, with streamwise slip, the flow is linearly stable to any perturbations, regardless of the slip length. In order to show evidences in a broader parameter regime, we numerically searched for the global maximum of $\max \lambda_r$ over α and n and explored a wider range of l_x up to 10 and of Re up to 10^6 . Practically, based

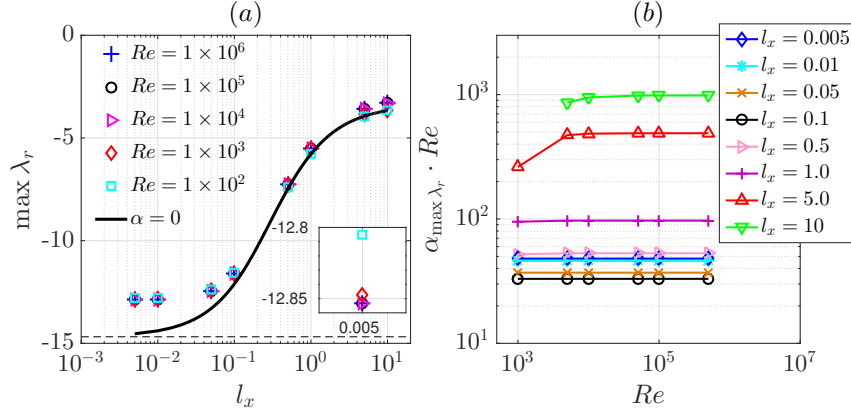


FIGURE 5. (a) The global maximum of $\max \lambda_r$, i.e. the maximum of $\max \lambda_r$ over α and n , for $Re = 100, 1000, 1 \times 10^4, 1 \times 10^5$, and 1×10^6 (symbols). The bold black line shows the maximum $\max \lambda_r$ of the $\alpha = 0$ modes, which is associated with the $(\alpha, n) = (0, 1)$ mode and is independent of Re . The dashed line marks the value for the $(\alpha, n) = (0, 1)$ mode in the no-slip case (Meseguer & Trefethen 2003). The inset shows the zoom-in at $l_x = 0.005$. (b) The product of Re and $\alpha_{\max \lambda_r}$ (the α at which $\max \lambda_r$ takes the maximum) plotted against Re .

on our analysis, we only need to search in a small range of α immediately above zero (see the insets in Figure 3) while setting $n = 1$. Specifically, the range of $[0, 1.2]$ is searched at $Re = 100$, and the range is decreased as Re^{-1} for higher Reynolds numbers. Then we plotted the global maximum of $\max \lambda_r$, still denoted as $\max \lambda_r$, as a function of l_x , for a few Reynolds numbers ranging from 10^2 to 10^6 in Figure 5(a).

It is interesting to note that our data for high Reynolds numbers all collapse over the whole l_x range investigated, see the cases with Re above 1×10^4 in Figure 5, suggesting that the maximum eigenvalue of the system is independent of Re . At lower Reynolds numbers, e.g. $Re = 100$ and 10^3 in the figure, there is almost a collapse for small l_x ($\lesssim 0.1$) but a small deviation from the high Reynolds number cases can be seen, see the inset that shows the zoom-in at $l_x = 0.005$. As l_x increases further, the maximum eigenvalue for $Re = 100$ and 10^3 approaches to that of $\alpha = 0$ modes, which is strictly Re -independent (see the proof in Section 5.1). Besides, the figure also shows that the global maximum of $\max \lambda_r$ is slightly larger than the maximum of the $\alpha = 0$ modes over the whole l_x range and the difference is most significant at small l_x . We did not explore further larger l_x considering that the range we investigated is already much larger than the slip length that can be encountered in applications ($\lesssim 0.1$ in set-ups with characteristic length of one millimeter or larger, because so far the maximum slip length achieved in experiments is $\mathcal{O}(100)$ micron, see Voronov *et al.* (2008); Lee *et al.* (2008); Lee & Jim (2009)). Nevertheless, the S -shaped trend as l_x increases suggests that the flow stays stable no matter how large the slip length is. In fact, as $l_x \rightarrow \infty$, full slip boundary condition is recovered, and the velocity profile of the base flow will be completely flat and no mean shear exists, in which case linear stability can be expected for any perturbations. Panel (b) shows the product of Re and the α at which $\max \lambda_r$ maximizes globally, denoted as $\alpha_{\max \lambda_r}$. Interestingly, it seems that this product is a constant when l_x is small ($\lesssim 0.1$) for all the Re 's investigated and approaches a constant as Re is sufficiently high ($\gtrsim 10^4$) if $l_x \gtrsim 0.1$. This indicates that $\alpha_{\max \lambda_r}$ scales as Re^{-1} for either not very large l_x or in high Reynolds number regime. It should be noted that we

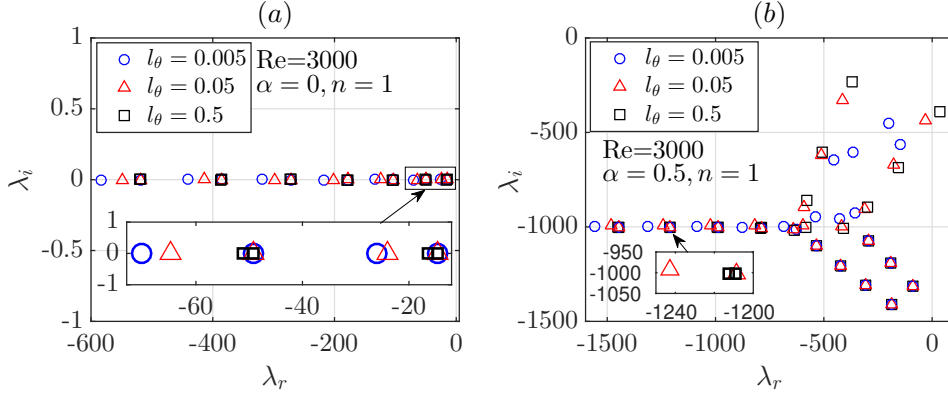


FIGURE 6. Spectrum of the flow at $Re = 3000$ with $l_\theta = 0.005$ (circles), 0.05 (triangles) and 0.5 (squares). (a) The mode $(\alpha, n) = (0, 1)$. (b) The mode $(\alpha, n) = (0.5, 1)$.

observed a non-monotonic dependence of $\alpha_{\max} \lambda_r \cdot Re$ on the slip length, which minimizes at around $l_x = 0.1$.

That the global $\max \lambda_r$ is Re -independent, as our results suggest, indicates that the slowest exponential decay rate (referred to as decay rate for simplicity hereafter) of perturbations scales as Re^{-1} given that the scaled time $\tau = \frac{t}{Re}$ is used in our formulation, see Eqs. (2.2). The same scaling was observed by the calculation of Meseguer & Trefethen (2003) for the $(\alpha, n) = (0, 1)$ mode of the classic pipe flow. Therefore, our results suggest that, as $Re \rightarrow \infty$, the decay rate of perturbations asymptotically approaches zero and stays negative, i.e. the flow is linearly stable at arbitrary Reynolds number. The Re^{-1} -scaling of the slowest decay rate can be rigorously proved for the $\alpha = 0$ modes, see Section 5.1.

In a word, in the pure streamwise slip case, we did not observe any linear instability in the large ranges of l_x and Re that we considered, and based on the data shown in Figure 5, we propose that streamwise slip destabilizes the flow but does not cause linear instability, regardless of the slip length and Reynolds number. A similar destabilizing effect was reported by Průša (2009) for the isotropic slip case.

4. Azimuthal slip

We consider the case of $l_\theta \neq 0$ and $l_x = 0$ as the limiting case of azimuthal slip being significant and streamwise slip being negligible.

The effect of azimuthal slip on the spectrum is investigated for $Re = 3000$ and is shown in Figure 6 for the modes $(\alpha, n) = (0, 1)$ and $(0.5, 1)$. Similar to the streamwise slip case, the eigenvalues of the $\alpha = 0$ mode also fall on the $\lambda_i = 0$ line and in the left half-plane, see panel (a). This suggests that the eigenvalues of streamwise-independent modes are all real and negative. We will show a rigorous proof of this observation in Section 5.1. As l_θ increases, similar to the streamwise slip case, we also observed two groups of eigenvalues. One group stays constant as the azimuthal slip length changes and the other shifts to the right, see the inset in panel (a). As we will theoretically show in Section 5.2 and 5.3, the former group is associated with the disturbances with $\Phi \equiv 0$ and is independent of l_θ , and the latter group is associated with the disturbances with $\Phi \neq 0$. The rightmost eigenvalue belongs to the former group for $l_\theta < 1$ and can only be overtaken by the latter group if $l_\theta > 1$ (the two groups precisely overlap when $l_\theta = 1$), i.e. the rightmost eigenvalue can

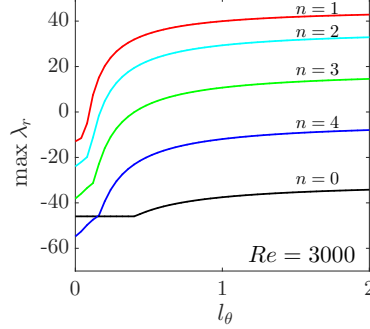


FIGURE 7. The $\max \lambda_r$ maximized over α , still denoted as $\max \lambda_r$, as a function of l_θ . Modes with $n = 0, 1, 2, 3$ and 4 are shown for $Re = 3000$.

only increase with l_θ if $l_\theta > 1$. For the $\alpha = 0.5$ and $n = 1$ mode, the mean-mode branch overall does not show either a vertical or horizontal shift, but adjacent eigenvalues are brought closer by the increasing slip length, and for $l_\theta = 0.5$ there is almost an eigenvalue degeneracy (see the inset in panel (b)). The center-mode branch is nearly unchanged as l_θ increases. However, the wall-mode branch is significantly affected. As l_θ increases, the wall mode overtakes the center mode and becomes the least stable perturbation, and as l_θ is sufficiently large, the rightmost eigenvalue appears in the right half-plane, indicating the onset of a linear instability. In contrast to the streamwise slip case, the wave speed of the mean modes does not change because the speed follows $\int_0^1 U_x(r) dr$ as aforementioned and the base flow $\mathbf{U}(r)$ is not affected by the azimuthal slip. The speed of the center modes is also not affected, whereas the wave speed of the wall modes is considerably decreased by the slip. This is reasonable because the slip boundary condition should mostly affect the flow close to the wall and should not affect significantly the flow far from the wall.

Figure 7 shows $\max \lambda_r$ maximized over α (over $[0, 2]$ in practice), still denoted as $\max \lambda_r$, as a function of l_θ for $n = 0, 1, 2, 3$ and 4 at $Re = 3000$. Overall, $\max \lambda_r$ increases monotonically as l_θ increases, while the $n = 0$ case seems to stay constant until it starts to increase at around $l_\theta = 0.4$. In the small l_θ regime, all modes are linearly stable. As l_θ is increased to around 0.1, $\max \lambda_r$ of the $n = 1$ mode becomes positive, indicating a linear instability. As l_θ increases further, $n = 2$ and 3 also become unstable. In the whole range of l_θ investigated, $n = 1$ is the least stable/most unstable one, which is also the case for other Reynolds numbers we investigated. Therefore, in the following, we mainly discuss about $n = 1$ modes.

Figure 8 shows $\max \lambda_r$ of modes $\alpha = 0.1, 0.5, 1.0$ and 2.0 for $Re = 3000$ and $n = 1$ as a function of l_θ . The results show that when l_θ is small, overall $\max \lambda_r$ decreases as α increases. As l_θ is increased, some moderate α turns to be the least stable/most unstable mode, see the crossover of $\alpha = 0.1$ (cyan thin line) and 0.5 (red dashed line) cases in the figure. Panel (b) shows the small l_θ range, in which it appears that $\max \lambda_r$ first stays nearly unchanged and then starts to increase, and the trend shows that the larger α , the later $\max \lambda_r$ starts to increase as l_θ is increased. The same behavior is also observed for $\alpha = 0$ modes and we will show a rigorous proof of this behavior in Section 5.3. Interestingly, the case of $\alpha = 2$ seems to stay unchanged up to $l_\theta = 2.0$.

The dependence of $\max \lambda_r$ on α is more comprehensively shown in Figure 9. The smallest $l_\theta = 0.005$ shows a monotonic decrease with increasing α , which completely

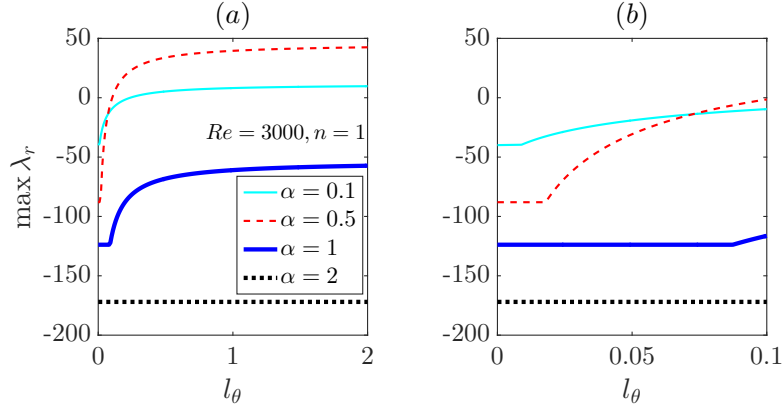


FIGURE 8. $\max \lambda_r$ of modes $\alpha = 0.1, 0.5, 1.0$ and 2.0 for $Re = 3000$ and $n = 1$ as a function of l_θ . Panel (b) shows the details in the small l_θ regime.

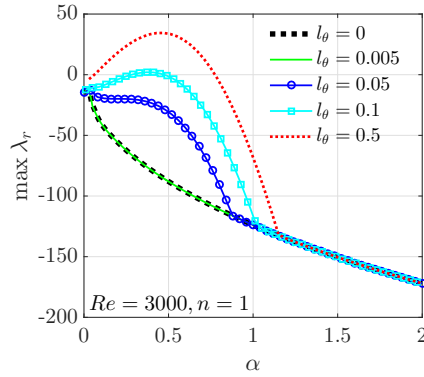


FIGURE 9. $\max \lambda_r$ of the $n = 1$ modes as a function of α for $Re = 3000$. The data for $l_\theta = 0, 0.005, 0.05, 0.1$ and 0.5 are plotted. Note that the curves for $l_\theta = 0$ (the black bold dotted line) and $l_\theta = 0.005$ (the green thin solid line) coincide.

collapses onto the curve for $l_\theta = 0$, i.e. the classic no-slip case. However, as l_θ increases, $\max \lambda_r$ significantly increases in the region of $0 < \alpha \lesssim 1$ such that a bump appears in the curves, see those for $l_\theta = 0.05, 0.1$ and 0.5 . At certain point, the bump reaches $\max \lambda_r = 0$ and the flow starts to become linearly unstable if l_θ increases further, see the cases of $l_\theta = 0.1$ and 0.5 . As observed in Figure 8 for the $\alpha = 2$ case, the results suggest that $\max \lambda_r$ of sufficiently large α seems unaffected by azimuthal slip in the l_θ range investigated, see the collapse of all curves above $\alpha \simeq 1.2$ in Figure 9. It should be noted that as l_θ becomes larger, the bump widens up, i.e. $\max \lambda_r$ is affected by the slip in a wider range of α .

Figure 10 shows the velocity field of the most unstable perturbation of mode $(\alpha, n) = (0.383, 1)$ for $Re = 3000$ with $l_\theta = 0.1$. Panel (a) shows the in-plane velocity field in the $r - \theta$ pipe cross-section and (b) shows the pattern of the streamwise velocity in the $x - r$ cross-section. The patterns shown suggest that the flow manifests with a pair of helical waves. The flow structures are mostly located near the wall ($r \gtrsim 0.5$), indicating that the most unstable mode is a wall-mode, which can also be seen in Figure 6(b).

Obviously, azimuthal slip can cause linear instability given sufficiently large slip length. We can search in the $l_\theta - \alpha$ plane to obtain the neutral stability curve for given Re and n .

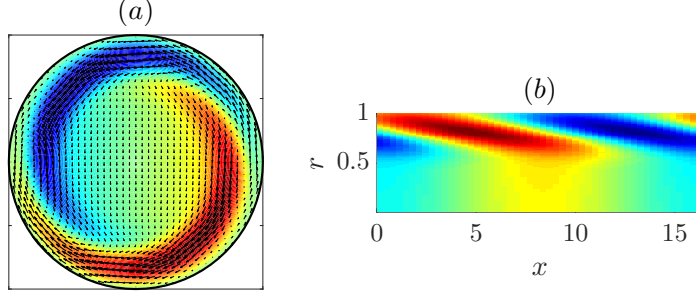


FIGURE 10. Visualization of the most unstable mode $(\alpha, n) = (0.383, 1)$ for $Re = 3000$ with $l_\theta = 0.1$. Panel (a) shows the $r - \theta$ cross-section and (b) the $x - r$ cross-section. In both panels, the streamwise velocity is plotted as the colormap with red color representing positive and blue representing negative values with respect to the base flow. In (a), the in-plane velocity field is plotted as arrows.

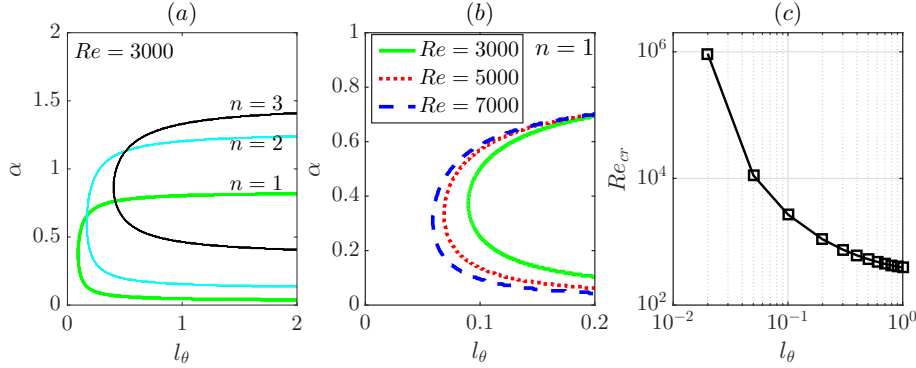


FIGURE 11. (a) The neutral stability curves for $Re = 3000$ and $n = 1, 2$ and 3 in the $l_\theta - \alpha$ plane. (b) The neutral stability curves for $n = 1$ and $Re = 3000, 5000$ and 7000 . (c) The critical Reynolds number Re_{cr} as a function of l_θ .

Figure 11(a) shows the neutral stability curves for $Re = 3000$ and $n = 1, 2$ and 3 ($n = 4$ and higher are all stable, see Figure 7). It can be seen that, as n increases, the unstable region shifts to the right and upward. However, as the results in Figure 7 show, $n = 1$ is the most unstable based on the eigenvalue maximized over α and therefore, we only investigate the $n = 1$ case in the following. Panel (b) shows the neutral stability curves for $n = 1$ and $Re = 3000, 5000$ and 7000 . As Re increases, the neutral stability curve moves towards the smaller l_θ region, indicating that, for a given l_θ , the flow becomes more unstable as Re increases, as expected. The data show that the wavelength of the unstable modes is comparable or significantly larger than the pipe diameter, whereas very long waves ($\alpha \rightarrow 0$) and short waves ($\alpha \gg 1.0$) are generally stable. That the flow is always stable to perturbations with $\alpha = 0$, regardless of the value of l_θ and Re , can be rigorously proved (see Section 5.1).

Further, for each l_θ , a critical Reynolds number Re_{cr} can be determined by searching the first appearance of a positive $\max \lambda_r$ in the $l_\theta - \alpha$ plane by varying Re . Figure 11(c) shows Re_{cr} as a function of l_θ . As shown, Re_{cr} is a few hundred if l_θ is large ($l_\theta \gtrsim 0.3$), but the trend suggests that it does not reduce to zero if $l_\theta \rightarrow \infty$. Since the classic pipe flow is linearly stable for arbitrary Reynolds number, there is an explosive increase in

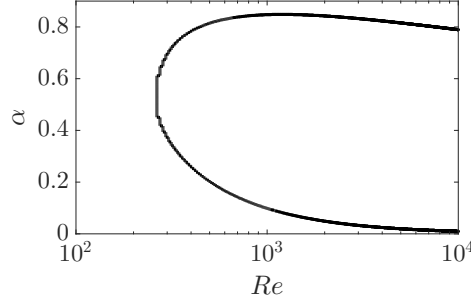


FIGURE 12. The neutral stability curve in the $Re - \alpha$ plane for $l_\theta = \infty$ and $n = 1$.

Re_{cr} as l_θ decreases, which can be expected because the classic pipe flow will be recovered if $l_\theta \rightarrow 0$. We also explored the limit of $l_\theta \rightarrow \infty$, in which case the boundary condition for the azimuthal velocity becomes the full slip condition of

$$\frac{\partial u_\theta}{\partial r} = 0. \quad (4.1)$$

The neutral stability curve for $n = 1$ in the $Re - \alpha$ plane is shown in Figure 12, which shows that the unstable modes are still long waves with α approximately between 0 and 0.8. The critical Reynolds number (the nose of the curve) appears approximately at $Re_{cr} = 260$.

5. Eigenvalues and eigenvectors of streamwise independent modes

We can rigorously prove the linear stability of the base flow to perturbations with $\alpha = 0$. In the following, we do not consider the $(\alpha, n) = (0, 0)$ mode, which should be strictly stable as it is purely dissipative and there can be no energy production mechanism associated with it. In fact, the stability of the classic pipe flow to streamwise independent perturbations has already been proved by Joseph & Hung (1971) using an energy analysis. Nevertheless, here we also account for the effect of the velocity slip and perform analytical studies on the eigenvalues and eigenvectors of $\alpha = 0$ modes.

5.1. Proof of linear stability to $\alpha = 0$ modes

For $\alpha = 0$, the eigenvalue λ of the operator $-M^{-1}L$ satisfies

$$\Gamma(n^2\Gamma)\Phi + \lambda\Gamma\Phi = 0, \quad (5.1)$$

and

$$\frac{2i}{1 + 4l_x}\Phi + \phi\Omega + \lambda n^2\Omega = 0, \quad (5.2)$$

where Φ and Ω compose the eigenvector \mathbf{q} associated with λ (see the definition of \mathbf{q} in (2.5)). The boundary conditions (2.10) and (2.11) reduce to

$$l_x\Omega' + \Omega = 0 \quad (5.3)$$

and

$$l_\theta\Phi'' + \Phi' = 0 \quad (5.4)$$

It can be seen that for $\alpha = 0$ modes, Ω and Φ are decoupled in the boundary conditions (5.3) and (5.4).

We define a space $\Theta = \{f|f \in C^2[0,1], f(0) = f(1) = 0\}$ and an inner product associated with this space

$$(f_1, f_2) = \int_0^1 r f_1 \bar{f}_2 dr, \quad (5.5)$$

where the over-bar represents complex conjugate. Then the operator Γ has the following two properties.

(a)

$$(\Gamma f_1, f_2) = (f_1, \Gamma f_2), \quad \forall f_1, f_2 \in \Theta, \quad (5.6)$$

Proof.

$$\begin{aligned} (\Gamma f_1, f_2) &= \int_0^1 r \left(\frac{f_1}{r^2} - \frac{1}{r} \frac{d}{dr} \left(\frac{r}{n^2} \frac{df_1}{dr} \right) \right) \bar{f}_2 dr \\ &= \int_0^1 \frac{f_1 \bar{f}_2}{r} dr - \int_0^1 \bar{f}_2 d \left(\frac{r}{n^2} \frac{df_1}{dr} \right) \\ &= \int_0^1 \frac{f_1 \bar{f}_2}{r} dr - \bar{f}_2 \left(\frac{r}{n^2} \frac{df_1}{dr} \right) \Big|_0^1 + \int_0^1 \frac{r}{n^2} \frac{df_1}{dr} d\bar{f}_2 \\ &= \int_0^1 \frac{f_1 \bar{f}_2}{r} dr + \int_0^1 \frac{r}{n^2} \frac{d\bar{f}_2}{dr} df_1 \end{aligned} \quad (5.7)$$

and similarly, using intergration by parts, it can be derived that

$$\begin{aligned} (f_1, \Gamma f_2) &= \int_0^1 r \left(\frac{\bar{f}_2}{r^2} - \frac{1}{r} \frac{d}{dr} \left(\frac{r}{n^2} \frac{d\bar{f}_2}{dr} \right) \right) f_1 dr \\ &= \int_0^1 \frac{f_1 \bar{f}_2}{r} dr + \int_0^1 \frac{r}{n^2} \frac{d\bar{f}_2}{dr} df_1 = (\Gamma f_1, f_2) \end{aligned} \quad (5.8)$$

□

(b)

$$(\Gamma f, f) \geq 0, \quad \forall f \in \Theta. \quad (5.9)$$

Proof. Taking $f = f_1 = f_2$ in Proof a,

$$(\Gamma f, f) = \int_0^1 \frac{f \bar{f}}{r} dr + \int_0^1 \frac{r}{n^2} \frac{d\bar{f}}{dr} df = \int_0^1 \frac{f \bar{f}}{r} dr + \int_0^1 \frac{r}{n^2} \frac{d\bar{f}}{dr} \frac{df}{dr} dr \geq 0. \quad (5.10)$$

□

Note that property (5.9) still holds for those f with $f(1) \neq 0$ but satisfy $f(1) + bf'(1) = 0$, where $b > 0$ is a constant, because

$$\begin{aligned} (\Gamma f, f) &= \int_0^1 \frac{f \bar{f}}{r} dr - f \left(\frac{r}{n^2} \frac{d\bar{f}}{dr} \right) \Big|_0^1 + \int_0^1 \frac{r}{n^2} \frac{d\bar{f}}{dr} df \\ &= \int_0^1 \frac{f \bar{f}}{r} dr + \int_0^1 \frac{r}{n^2} \frac{d\bar{f}}{dr} \frac{df}{dr} dr + \frac{1}{bn^2} f(1) \bar{f}(1) \geq 0. \end{aligned} \quad (5.11)$$

Firstly, for the case of $\Phi \equiv 0$ (i.e. the wall normal velocity component $u_r \equiv 0$) and $\Omega \neq 0$, Eqs. (5.2) becomes

$$\phi \Omega + \lambda n^2 \Omega = 0, \quad (5.12)$$

and the operators ϕ and Γ are related as $\phi = \frac{n^4}{r^2} - \frac{1}{r} \frac{d}{dr} \left(n^2 r \frac{d}{dr} \right) = n^4 \Gamma$. Therefore,

Eqs. (5.12) becomes

$$n^4\Gamma\Omega + \lambda n^2\Omega = 0. \quad (5.13)$$

Taking the inner product of Eqs. (5.13) with Ω , we have

$$(n^4\Gamma\Omega, \Omega) + (\lambda n^2\Omega, \Omega) = 0. \quad (5.14)$$

According to property (5.9), $(n^4\Gamma\Omega, \Omega) \geq 0$ given $\Omega(1) = 0$ (without streamwise slip) or $\Omega(1) + l_x\Omega'(1) = 0$ (with streamwise slip), which leads to $\lambda < 0$, i.e. the eigenvalue is real and negative.

Secondly, we discuss about the $\Phi \neq 0$ case, i.e. the wall normal velocity component $u_r \neq 0$. From Eqs. (5.1), by denoting $g = n^2\Gamma\Phi + \lambda\Phi$, we have $\Gamma g = 0$, i.e.

$$n^2g = r(rg')', \quad (5.15)$$

from which it can be obtained that

$$r^n g = Cr^{2n} + C_1, \quad (5.16)$$

where C and C_1 are constants. Note that for $n = 2$, $r^2g = n^2r^2\Gamma\Phi + \lambda r^2\Phi = n^2\Phi - nr(r\Phi')'$ has to vanish at $r = 0$, because Φ vanishes, and Φ' and Φ'' are finite at $r = 0$. The same applies to $n > 2$. If $n = 1$, $rg = \frac{\Phi}{r} - (r\Phi')' + \lambda r\Phi = \frac{\Phi}{r} - \Phi' - r\Phi'' + \lambda r\Phi$, which also vanishes when $r \rightarrow 0$ (using L'Hopital rule). Therefore, $C_1 \equiv 0$ and $r^n g = Cr^{2n}$, i.e.

$$n^2\Gamma\Phi + \lambda\Phi = Cr^n. \quad (5.17)$$

5.1.1. The case without azimuthal slip, i.e. $l_\theta = 0$

In case of $l_\theta = 0$, the boundary condition (2.11) or (5.4) becomes $\Phi' = 0$. Taking the inner product (5.5) of Eqs. (5.17) and $\Gamma\Phi$, we have

$$n^2(\Gamma\Phi, \Gamma\Phi) + \lambda(\Phi, \Gamma\Phi) = C(r^n, \Gamma\Phi) = C(\Gamma r^n, \Phi) = C(0, \Phi) = 0. \quad (5.18)$$

The second equality in Eqs. (5.18) holds in spite of that $r^n \notin \Theta$ and thus, property (5.6) cannot be applied directly. Nevertheless, as $\Phi = \Phi' = 0$ at $r = 1$ in case of $l_\theta = 0$, property (5.6) still holds (this can be seen by taking Φ as f_2 and r^n as f_1 in Proof a). What follows is that the eigenvalue λ is real and $\lambda < 0$ because $(\Gamma\Phi, \Gamma\Phi) > 0$ and $(\Phi, \Gamma\Phi) > 0$.

5.1.2. The case with azimuthal slip, i.e. $l_\theta \neq 0$

In case of $l_\theta \neq 0$, Eqs. (5.18) does not hold, except for $C = 0$, because $\Phi' = 0$ at $r = 1$ does not necessarily hold and therefore the second equality in Eqs. (5.18) does not hold either. For $C \neq 0$, consider the special case of $C = 1$ (if $C \neq 1$, a rescaling of $\tilde{\Phi} = \Phi/C$ can easily convert to this special case), Eqs. (5.17) can be written as

$$(n^2 + \lambda r^2)\Phi - r(r\Phi')' = (n^2 + \lambda r^2)\Phi - r(\Phi' + r\Phi'') = r^{n+2}. \quad (5.19)$$

As $r \rightarrow 1$, Eqs. (5.19) turns to

$$-(\Phi' + \Phi'') = 1. \quad (5.20)$$

Further, the azimuthal slip requires

$$\Phi'(1) + l_\theta\Phi''(1) = 0, \quad l_\theta \in (0, +\infty). \quad (5.21)$$

It follows that, for $l_\theta = 1$, C has to be zero, otherwise Eqs. (5.20) and (5.21) would conflict with each other. That $C = 0$ leads to $\lambda < 0$, see Eqs. (5.18). For $l_\theta \neq 1$, one can

solve for Φ' from Eqs. (5.20) and (5.21) as

$$\Phi'(1) = \frac{l_\theta}{1 - l_\theta}, \quad (5.22)$$

which indicates that $\Phi'(1)$ is real and $\Phi'(1) \in (-\infty, -1) \cup (0, +\infty)$.

It can be verified that Eqs. (5.19) has a special solution

$$\Phi = \frac{r^n}{\lambda}, \quad (5.23)$$

and its corresponding homogeneous differential equation is

$$r^2\Phi'' + r\Phi' - (n^2 + \lambda r^2)\Phi = 0. \quad (5.24)$$

From the theory of ordinary differential equation, this equation has two linearly independent solutions in $(0, 1]$. One of the two solutions can be represented as a generalized power series

$$\Phi_1 = \sum_{m=0}^{\infty} B_m r^{m+\rho} \quad (B_0 \neq 0), \quad (5.25)$$

in which it can be obtained that $\rho = n$, $B_{2k+1} = 0$ and $B_{2k} = \left(\frac{\lambda}{4}\right)^k \frac{B_0}{k!(n+k)!}$ using the standard undetermined coefficient method. Denoting $a_n = B_0$, Eqs. (5.25) can be written as

$$\Phi_1 = a_n r^n \sum_{k=0}^{\infty} \left(\frac{\lambda}{4}\right)^k \frac{r^{2k}}{k!(n+k)!}. \quad (5.26)$$

The other solution of Eqs. (5.24) has the following form

$$\Phi_2 = \Phi_1 \int_1^r \frac{1}{\Phi_1^2(s)} \exp\left(-\int_1^s \frac{1}{t} dt\right) ds = \Phi_1 \int_1^r \frac{1}{s\Phi_1^2(s)} ds. \quad (5.27)$$

However, by L'Hopital rule,

$$\lim_{r \rightarrow 0} \Phi_2(r) = \lim_{r \rightarrow 0} \frac{\int_1^r \frac{1}{s\Phi_1^2(s)} ds}{\frac{1}{\Phi_1(r)}} = \lim_{r \rightarrow 0} \frac{\frac{1}{r\Phi_1^2(r)}}{\frac{\Phi_1'(r)}{\Phi_1^2(r)}} = \infty, \quad (5.28)$$

which is unphysical, and therefore Φ_2 should not appear in the general solution of Eqs. (5.19), i.e. the general solution of Eqs. (5.19) can be solved as

$$\Phi = \frac{1}{\lambda} r^n + a_n r^n \sum_{k=0}^{\infty} \left(\frac{\lambda}{4}\right)^k \frac{r^{2k}}{k!(n+k)!}. \quad (5.29)$$

For simplicity, denoting $\mu = \frac{\lambda}{4}$ and using the boundary condition $\Phi(1) = 0$, one can solve for a_n as

$$a_n = -\frac{1}{4\mu} \left(\sum_{k=0}^{\infty} \frac{\mu^k}{k!(n+k)!} \right)^{-1}, \quad (5.30)$$

consequently,

$$\begin{aligned}\Phi'(1) &= \frac{n}{4\mu} + a_n \sum_{k=0}^{\infty} \frac{\mu^k (n+2k)}{k!(n+k)!} \\ &= -\frac{1}{4\mu} \left(\sum_{k=0}^{\infty} \frac{\mu^k}{k!(n+k)!} \right)^{-1} \sum_{k=0}^{\infty} \frac{2k\mu^k}{k!(n+k)!},\end{aligned}\quad (5.31)$$

i.e. μ satisfies

$$\sum_{k=1}^{\infty} \frac{k\mu^{k-1}}{k!(n+k)!} + 2\Phi'(1) \sum_{k=0}^{\infty} \frac{\mu^k}{k!(n+k)!} = 0. \quad (5.32)$$

In the following, we prove that μ has to be real and $\mu < 0$ given Eqs. (5.32). For simplicity, let $s = \Phi'(1)$ and define $f(z)$ as

$$f(z) = \sum_{k=0}^{\infty} \frac{z^k}{k!(n+k)!}, \quad (5.33)$$

where z is complex. Then, Eqs. (5.32) states that μ is a root of the equation $f'(z) + 2sf(z) = 0$. Note that

$$(z^{n+1}f'(z))' = \left(\sum_{k=1}^{\infty} \frac{kz^{n+k}}{k!(n+k)!} \right)' = z^n \sum_{k=1}^{\infty} \frac{z^{n-k}}{(k-1)!(n+k-1)!} = z^n \sum_{k=0}^{\infty} \frac{z^k}{k!(n+k)!} = z^n f(z). \quad (5.34)$$

Then, defining $f_{\mu}(z) = f(\mu z)$, it can be verified that

$$(z^{n+1}f'_{\mu}(z))' = \mu z^n f_{\mu}(z), \quad (5.35)$$

in which the prime denotes the derivative with respect to z . Further, note that $\bar{\mu}$ is also a root of Eqs. (5.32), because the coefficients are all real. That is to say,

$$(z^{n+1}f'_{\bar{\mu}}(z))' = \bar{\mu} z^n f_{\bar{\mu}}(z), \quad (5.36)$$

where $f_{\bar{\mu}} = f(\bar{\mu}z)$. Then, the difference between Eqs (5.35) multiplied by $f_{\bar{\mu}}(z)$ and Eqs. (5.36) multiplied by $f_{\mu}(z)$, integrated along the real axis from 0 to 1 gives that

$$\begin{aligned}& \int_0^1 (z^{n+1}f'_{\mu}(z))' f_{\bar{\mu}}(z) dz - \int_0^1 (z^{n+1}f'_{\bar{\mu}}(z))' f_{\mu}(z) dz \\ &= z^{n+1}f'_{\mu}(z)f_{\bar{\mu}}(z) \Big|_0^1 - \int_0^1 z^{n+1}f'_{\mu}(z) df_{\bar{\mu}}(z) - z^{n+1}f'_{\bar{\mu}}(z)f_{\mu}(z) \Big|_0^1 + \int_0^1 z^{n+1}f'_{\bar{\mu}}(z) df_{\mu}(z) \\ &= \int_0^1 z^{n+1}|f'_{\mu}(z)|^2 dz - \int_0^1 z^{n+1}|f'_{\bar{\mu}}(z)|^2 dz + f'_{\mu}(1)f_{\bar{\mu}}(1) - f_{\mu}(1)f'_{\bar{\mu}}(1) \\ &= 2s(\bar{\mu} - \mu)|f_{\mu}(1)|^2 = (\mu - \bar{\mu}) \int_0^1 z^n |f_{\mu}(z)|^2 dz,\end{aligned}$$

where the condition $f'(z) + 2sf(z) = 0$ is used to derive $f'_{\mu}(z) + 2\mu s f_{\mu}(z) = 0$ and $f'_{\bar{\mu}}(z) + 2\bar{\mu} s f_{\bar{\mu}}(z) = 0$. Then we have

$$(\mu - \bar{\mu}) \left(\int_0^1 z^n |f_{\mu}(z)|^2 dz + 2s|f_{\mu}(1)|^2 \right) = 0. \quad (5.37)$$

Similarly, the sum of Eqs (5.35) multiplied by $f_{\bar{\mu}}(z)$ and Eqs. (5.36) multiplied by

$f_\mu(z)$, integrated along the real axis from 0 to 1 gives that

$$(\mu + \bar{\mu}) \left(\int_0^1 z^n |f_\mu(z)|^2 dz + 2s |f_\mu(1)|^2 \right) = -2 \int_0^1 z^{n+1} |f'_\mu(z)|^2 dz, \quad (5.38)$$

which indicates $\int_0^1 z^n |f_\mu(z)|^2 dz + 2s |f_\mu(1)|^2 \neq 0$ because the right hand side is non-zero. Consequently, Eqs. (5.37) indicates that $\mu - \bar{\mu} = 0$, i.e. μ is real.

Subsequently, we can deduce that $\mu < 0$ if $s \in (0, \infty)$ because the term in the parentheses and the integral on the right hand side of Eqs. (5.38) are all positive. In case of $s \in (-\infty, -1)$, if μ were positive, one would obtain

$$-2s \sum_{k=0}^{\infty} \frac{\mu^k}{k!(n+k)!} = \sum_{k=1}^{\infty} \frac{k\mu^{k-1}}{k!(n+k)!} = \sum_{k=0}^{\infty} \frac{\mu^k}{k!(n+k+1)!} \leq \sum_{k=0}^{\infty} \frac{\mu^k}{k!(n+k)!}, \quad (5.39)$$

and consequently $-2s \leq 1$, which would conflict with $s \in (-\infty, -1)$. Therefore, $\mu < 0$. Finally, we obtain that $\mu < 0$ for $s \in (-\infty, -1) \cup (0, +\infty)$, i.e. for any value of $l_\theta \neq 1$. Since we have shown before that $\lambda < 0$ for $l_\theta = 1$ and for $l_\theta = 0$, now we reach the conclusion that λ is real and $\lambda < 0$ for any $l_\theta \in [0, +\infty)$, regardless of l_x , i.e. the flow is rigorously linearly stable to perturbations with $\alpha = 0$ with or without velocity slip.

5.2. Analytical solution of the eigenvalue and eigenvector for $\alpha = 0$ modes

We consider the general case with both streamwise and azimuthal slip. For $\Phi \neq 0$, if $C \neq 0$, we obtain from Eqs. (5.32) that $\mu = \frac{\lambda}{4}$ satisfies

$$(1 - l_\theta) \sum_{k=1}^{\infty} \frac{k\mu^{k-1}}{k!(n+k)!} + 2l_\theta \sum_{k=0}^{\infty} \frac{\mu^k}{k!(n+k)!} = 0, \quad (5.40)$$

where Eqs. (5.22) is used. The Bessel functions of integer order n and $n+1$ read

$$J_n(z) = \sum_{k=0}^{\infty} \frac{(-1)^k}{k!(n+k)!} \left(\frac{z}{2}\right)^{2k+n} = \left(\frac{z}{2}\right)^n \sum_{k=0}^{\infty} \frac{1}{k!(n+k)!} \left(-\frac{z^2}{4}\right)^k, \quad (5.41)$$

$$J_{n+1}(z) = \sum_{k=0}^{\infty} \frac{(-1)^k}{k!(n+1+k)!} \left(\frac{z}{2}\right)^{2k+n+1} = \left(\frac{z}{2}\right)^{n+1} \sum_{k=0}^{\infty} \frac{1}{k!(n+k+1)!} \left(-\frac{z^2}{4}\right)^k. \quad (5.42)$$

Denoting $\mu = -\frac{\eta^2}{4}$, i.e. the eigenvalue $\lambda = 4\mu = -\eta^2$, it can be observed that η is a root of the equation

$$(1 - l_\theta)J_{n+1}(z) + l_\theta z J_n(z) = 0. \quad (5.43)$$

Next, we show that $C \neq 0$ if $l_\theta \neq 1$. Assuming $C = 0$ and $l_\theta \neq 1$, $\Phi'(1) + \Phi''(1) = 0$ and the boundary condition $\Phi'(1) + l_\theta \Phi''(1) = 0$ would give $\Phi'(1) = \Phi''(1) = 0$. Recall that the solution to the homogeneous equation Eqs. (5.24) is

$$\Phi_1 = a_n r^n \sum_{k=0}^{\infty} \left(\frac{\lambda}{4}\right)^k \frac{r^{2k}}{k!(n+k)!}, \quad (5.44)$$

where a_n is a constant. Using the notation of (5.33), $f(\mu) = \sum_{k=0}^{\infty} \mu^k \frac{1}{k!(n+k)!} = 0$ results from $\Phi_1(1) = 0$ (note that $\Phi = \Phi_1$ if $C = 0$), which would indicate that the

corresponding η satisfies $J_n(z) = 0$. Further, $\Phi'(1) = 0$ gives

$$\sum_{k=0}^{\infty} \mu^k \frac{n+2k}{k!(n+k)!} = 0. \quad (5.45)$$

In combination with $f(\mu) = 0$, we would obtain that

$$\sum_{k=1}^{\infty} \mu^k \frac{1}{(k-1)!(n+k)!} = \sum_{k=0}^{\infty} \mu^k \frac{1}{k!(n+k+1)!} = 0, \quad (5.46)$$

which means that η would also be a zero of $J_{n+1}(z)$, i.e. η would be a zero of both $J_n(z)$ and $J_{n+1}(z)$. This would conflict with the fact that there exists no common zero of $J_n(z)$ and $J_{n+1}(z)$. Therefore, $C \neq 0$ and η is a root of Eqs. (5.43) if $l_\theta \neq 1$.

We have proved before that $C = 0$ if $l_\theta = 1$, which gives $\Phi = \Phi_1$. Consequently, $\Phi(1) = \Phi_1(1) = 0$ gives $f(\mu) = 0$, which means η is a root of $J_n(z) = 0$, i.e. η is also a root of Eqs. (5.43) (note that the first term disappears if $l_\theta = 1$). Therefore, η is a root of Eqs. (5.43) for any $l_\theta \geq 0$.

For the case of $\Phi \equiv 0$, Eqs. (5.13) and the corresponding boundary condition $\Omega(1) + l_x \Omega'(1) = 0$ (see Eqs. (2.11) and (5.3)) imply that the eigenvector Ω has the same form as the solution Φ_1 , and we can deduce that $\lambda = -\gamma^2$, in which γ is a root of

$$(1 + nl_x)J_n(z) - l_x z J_{n+1}(z) = 0. \quad (5.47)$$

For an eigenvalue $\lambda = -\eta^2$, the corresponding eigenvector can be solved as

$$\Phi = J_n(\eta r) - J_n(\eta) r^n, \quad (5.48)$$

$$\Omega = b_n J_n(\eta r) + \frac{2i}{(1 + 4l_x)n^2} \left(\frac{r}{2\eta} J_{n+1}(\eta r) - \frac{J_n(\eta)}{\eta^2} r^n \right), \quad (5.49)$$

where b_n is a constant and should be determined by the boundary condition Eqs. (5.3). For an eigenvalue $\lambda = -\gamma^2$, the eigenvector can be solved as

$$\Phi \equiv 0, \quad \Omega = J_n(\gamma r). \quad (5.50)$$

To sum up, there are always two groups of eigenvalues, corresponding to $\Phi \equiv 0$ (given by Eqs. 5.47) and $\Phi \neq 0$ (given by Eqs. 5.43), respectively. Particularly, for the no-slip case, Eqs. (5.43) reduces to $J_{n+1}(z) = 0$ and Eqs. (5.47) reduces to $J_n(z) = 0$, and it is known that the zeros of $J_n(z)$ and $J_{n+1}(z)$ distribute alternately. Therefore, in the no-slip case, these two groups of eigenvalues distribute alternately either. For the streamwise slip case, Eqs. (5.43) still reduces to $J_{n+1}(z) = 0$, i.e. the $\Phi \neq 0$ eigenvalues do not change with l_x , whereas the $\Phi \equiv 0$ eigenvalues will change with l_x . However, there cannot be common roots between $J_{n+1}(z) = 0$ and Eqs. 5.47, otherwise there would be common zeros between $J_n(z)$ and $J_{n+1}(z)$, which conflicts with the fact that there are none common zero between the two. Therefore, as l_x changes, the two groups of eigenvalues distribute in the same alternating pattern as in the no-slip case and there is no over-taking between the two groups, see Figure 1(a) and Figure 13(a). However, this behavior is not guaranteed in the azimuthal slip case as there can be common roots between Eqs. (5.43) and (5.47) given $l_x = 0$ and $l_\theta = 1.0$, i.e. the roots of $J_n(z) = 0$. Nonetheless, it should be noted that the common roots can only exist at $l_\theta = 1.0$. This implies that, when eigenvalues change with l_θ , an over-taking between the two groups may occur at precisely $l_\theta = 1.0$.

Figure 13 shows the comparison between our analytical solution of the two groups of eigenvalues and numerical calculation for the streamwise slip case of $Re = 3000$,

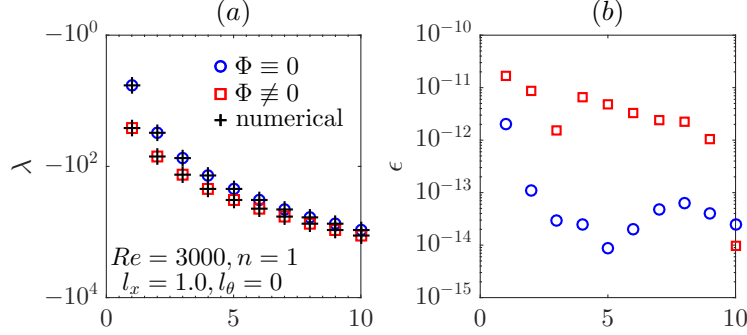


FIGURE 13. Validation of the analytical eigenvalues against the numerical calculation for the case of $Re = 3000$, $n = 1$, $l_x = 1.0$ and $l_\theta = 0$. In (a), the first 20 eigenvalues are shown as squares and circles, and the numerical results are shown as crosses. The circles are the first ten eigenvalues (in descending order) for the cases with $\Phi \equiv 0$ and the squares are the first 10 eigenvalues (in descending order) for the $\Phi \neq 0$ case. (b) The relative error ϵ between the analytical and numerical ones.

$n = 1$, $l_x = 1.0$ and $l_\theta = 0$. In panel (a), blue circles are analytical solutions of the first 10 largest eigenvalues given by Eqs. (5.47), i.e. the corresponding eigenvectors all have $\Phi \equiv 0$, and red squares represent the first 10 largest eigenvalues given by Eqs. (5.43), i.e. the corresponding eigenvectors all have $\Phi \neq 0$. Clearly, the leading eigenvalue is and will always be associated with $\Phi \equiv 0$ disturbances because no over-taking between the two groups of eigenvalues can occur as l_x varies, as we concluded in Section 5.2. These analytical solutions agree very well with the numerical calculations (the crosses) with relative errors of $\mathcal{O}(10^{-11})$ or lower, see panel (b). The eigenvector associated with the leading eigenvalue (the leftmost circle in Figure 13(a)) is plotted in Figure 14(a). The black line shows the analytical solution given by (5.50) and the circles show the numerical calculation. The Φ part of the eigenvector is not shown because $\Phi \equiv 0$. Figure 14(b) shows the eigenvector associated with the second largest eigenvalue (the leftmost red square in Figure 13(a)), which has a non-zero Φ part. The figure shows that, for both Φ and Ω , our analytical solutions (lines) agree very well with the numerical calculations (symbols). This comparison validates our theory about the eigenvalue and eigenvector.

The two groups of eigenvalues of the azimuthal slip cases of $l_\theta = 0.05$ and 2.0 for $Re = 3000$, $n = 1$ and $l_x = 0$ are also shown in Figure 15. Again, perfect agreement between the analytical and numerical ones is observed. We can see that, for $l_\theta = 0.05$, the $\Phi \neq 0$ group is entirely below the $\Phi \equiv 0$ group, which is independent of l_θ , whereas is entirely above the $\Phi \equiv 0$ group for $l_\theta = 2.0$, indicating that an over-taking indeed occurs between the two groups as l_θ increases. Therefore, for $l_\theta < 1.0$, the leading eigenvalue is associated with $\Phi \equiv 0$ disturbances and does not change with l_θ (see also Figure 6(a)), whereas it is associated with $\Phi \neq 0$ disturbances and increases with l_θ for $l_\theta > 1.0$.

5.3. The dependence of the leading eigenvalue on slip length for $\alpha = 0$ modes

Denoting $F(z, l_\theta) = (1 - l_\theta)J_{n+1}(z) + l_\theta z J_n(z)$, it can be obtained that, as $z \rightarrow 0$,

$$J_n(z) \sim \frac{z^n}{2^n n!}, \quad F(z, l_\theta) \sim \left(\frac{1 - l_\theta}{2^{n+1}(n+1)!} + \frac{l_\theta}{2^n n!} \right) z^{n+1}. \quad (5.51)$$

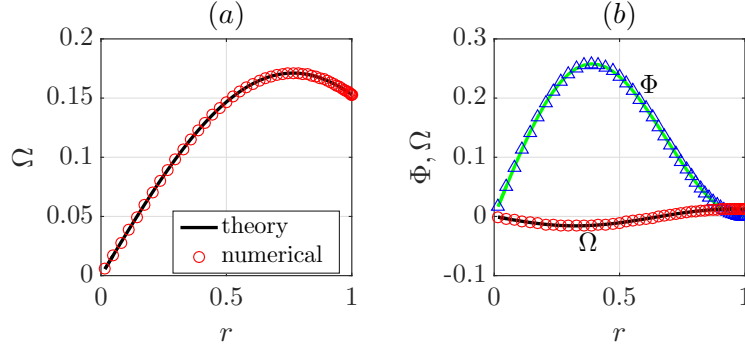


FIGURE 14. Validation of the analytical eigenvectors against the numerical calculation for the case of $Re = 3000$, $n = 1$, $l_x = 1.0$ and $l_\theta = 0$. (a) The Ω component of the eigenvector associated with the leading eigenvalue (the leftmost blue circle in Figure 13(a)). The Φ component is zero and is not shown. (b) The Ω and Φ component of the eigenvector associated with the second largest eigenvalue (the leftmost red square in Figure 13(a)).

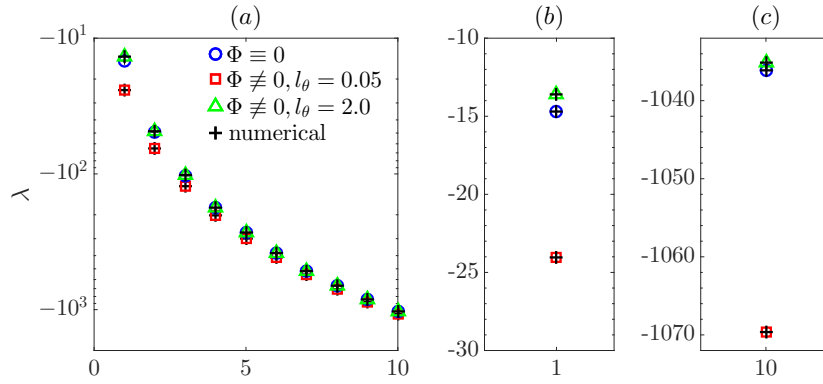


FIGURE 15. Eigenvalues for $Re = 3000$, $n = 1$ and $l_x = 0$ with $l_\theta = 0.05$ and 2.0 . In (a), analytical eigenvalues are shown as circles ($\Phi \equiv 0$, for which eigenvalues are independent of l_θ), squares ($\Phi \neq 0$ and $l_\theta = 0.05$) and triangles ($\Phi \neq 0$ and $l_\theta = 2.0$), and the numerical calculations are shown as crosses. Panel (b) and (c) show the zoom-in of the two ends of the spectrum shown in (a).

It can be seen that $\frac{1-l_\theta}{2^{n+1}(n+1)!} + \frac{l_\theta}{2^n n!} > 0$ for $l_\theta \geq 0$, therefore, $F(z, l_\theta)$ is positive for sufficiently small z . Let z_1 be the minimum root of $F(z, l_{\theta 1}) = 0$ and z_2 be the minimum root of $F(z, l_{\theta 2}) = 0$. If $l_{\theta 1} < l_{\theta 2}$, it can be derived that

$$\begin{aligned}
 F(z_1, l_{\theta 2}) &= (1 - l_{\theta 2})J_{n+1}(z_1) + l_{\theta 2}z_1J_n(z_1) \\
 &= (1 - l_{\theta 2})J_{n+1}(z_1) - \frac{1 - l_{\theta 1}}{l_{\theta 1}}l_{\theta 2}J_{n+1}(z_1) \\
 &= \frac{l_{\theta 1} - l_{\theta 2}}{l_{\theta 1}}J_{n+1}(z_1) < 0.
 \end{aligned} \tag{5.52}$$

In (5.52), $J_{n+1}(z) > 0$ follows from that, at the minimum positive zero of $J_{n+1}(z)$, denoted as z_0 , we have $F(z_0, l_{\theta 1}) < 0$ because $J_n(z_0) < 0$. We showed before that $F(z, l_{\theta 1}) > 0$ at sufficiently small z , therefore, the minimum positive zero of $F(z, l_{\theta 1})$, z_1 , should be smaller than z_0 given that $F(z, l_{\theta 1})$ is continuous with respect to z , i.e. $z_1 < z_0$, and therefore $J_{n+1}(z_1) > 0$. Consequently, given $F(z_1, l_{\theta 2}) < 0$, there must be

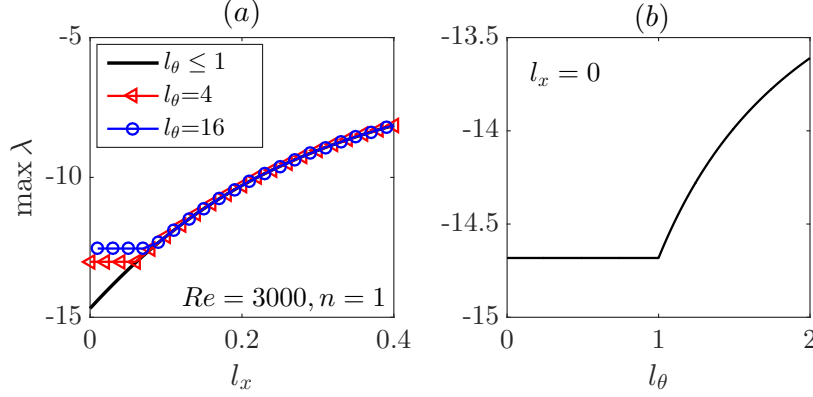


FIGURE 16. The dependence of $\max \lambda$ on slip length for $Re = 3000$ and $n = 1$. (a) Both streamwise and azimuthal slip are present. The black line shows the dependence on l_x given $l_\theta \leq 1$. Symbol lines show two cases for $l_\theta > 1$. (b) The dependence on l_θ in case of $l_x = 0$.

a zero in $(0, z_1)$, i.e. $z_2 < z_1$ because the function $F(z, l_{\theta 2})$ is continuous with respect to z . This states that, for the case of $\Phi \neq 0$, the maximum eigenvalue λ , denoted as λ_1 in the following, increases as l_θ increases and is independent of l_x . Similarly, one can deduce that the minimum root of Eqs. (5.47) decreases as l_x increases, consequently, the maximum eigenvalue for the $\Phi \equiv 0$ case, denoted as λ_2 , increases as l_x increases and is independent of l_θ . For the special case of $l_x = 0$, Eqs. (5.47) becomes $J_n(z) = 0$ and for the case of $l_\theta = 1$, Eqs. (5.43) turns into $zJ_n(z) = 0$. Clearly, these two cases share the non-zero roots, i.e. $\lambda_1 = \lambda_2$. Therefore, the minimum root of Eqs. (5.47) is always greater than that of Eqs. (5.43), i.e. $\lambda_1 > \lambda_2$, when $l_\theta < 1$. This explains why, for a given $l_\theta \leq 1$, $\max \lambda$ increases monotonically as l_x increases from zero, whereas for a given $l_\theta > 1$, $\max \lambda$ first stays constant and only starts to increase until l_x is increased above a threshold, see Figure 16(a). If only azimuthal slip is present, i.e. $l_x = 0$, $\max \lambda$ firstly stays constant and only starts to increase precisely at $l_\theta = 1$, see Figure 16(b). The data shown in the inset of Figure 6(a) also support this conclusion, see that $\max \lambda$ for $l_\theta = 0.005, 0.05$ and 0.5 are identical. It can also be inferred that, given a fixed $l_x > 0$ and that λ_2 increases with l_x , $\max \lambda$ can only start to increase as l_θ increases at some $l_\theta > 1$.

In summary, the maximum eigenvalue of $\alpha = 0$ modes is an increasing function of l_θ or l_x (may not be strictly increasing, depending on the slip length setting, as Figure 16 shows) and is independent of the Reynolds number, which is obvious as Re does not appear in Eqs. (5.43) and (5.47). Nevertheless, the eigenvalues remain negative.

6. Non-modal stability

It has been known that in many shear flows (e.g., pipe, channel and plane-Couette flows), small disturbances can be transiently amplified due to the non-normality of the linearized equations, despite their asymptotic linear stability (Schmid & Henningson 1994; Meseguer & Trefethen 2003; Schmid 2007). This transient amplification is believed to play an important role in the subcritical transition in shear flows. Here, we also investigated the effects of the anisotropic slip on the non-modal stability of the flow. The same method for calculating the transient growth described by Schmid & Henningson (1994) is adopted. The transient growth at time t for a mode (α, n) is defined as

$$G(t; \alpha, n) = \max_{E(0) \neq 0} \frac{E(t)}{E(0)}, \quad (6.1)$$

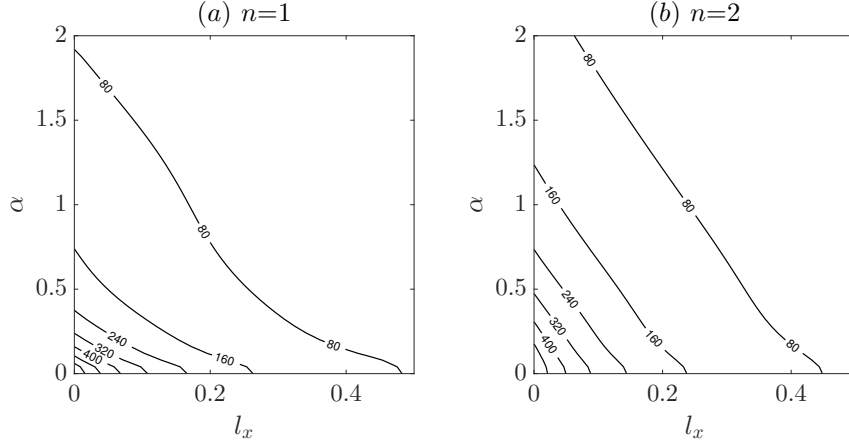


FIGURE 17. The maximum transient growth, G_{max} , at $Re = 3000$ plotted in the l_x - α plane for $n = 1$ (a) and $n = 2$ (b). Azimuthal slip length $l_\theta=0$. The contour level step is 80 in both panels.

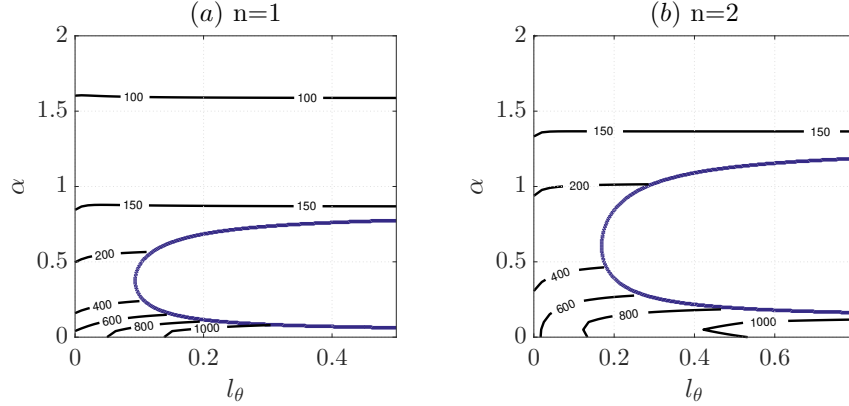


FIGURE 18. The maximum transient growth, G_{max} , at $Re = 3000$ plotted in the l_θ - α plane for $n = 1$ (a) and $n = 2$ (b). Streamwise slip length $l_x=0$. The bold lines enclose the linearly unstable regions.

where $E(t) = \int_V \mathbf{u}(t)^2 dV$ is the kinetic energy of the perturbation \mathbf{u} integrated in the whole flow domain at time t . For linearly stable flow, G will reach the maximum, G_{max} , at certain time and monotonically decay at larger times. For linearly unstable flow, G can be either non-monotonic or monotonic at early stages, depending on the competition between the modal and non-modal growth, and will be dominated by the exponential growth of the most unstable disturbance at large times.

Figure 17 shows G_{max} at $Re = 3000$ in the l_x - α plane ($l_\theta = 0$) for $n = 1$ and $n = 2$ (low azimuthal wavenumbers are generally most amplified by non-normality). From the contour lines we can see that streamwise slip reduces G_{max} and the decrease is monotonic as l_x increases. Intuitively, streamwise slip reduces the background shear such that the lift-up mechanism (Brandt 2014) is subdued. Therefore, the transient growth should be reduced as our results show. The most amplified mode is still the $(\alpha, n) = (0, 1)$ mode (streamwise rolls) as in the no-slip case (Schmid & Henningson 1994; Meseguer & Trefethen 2003).

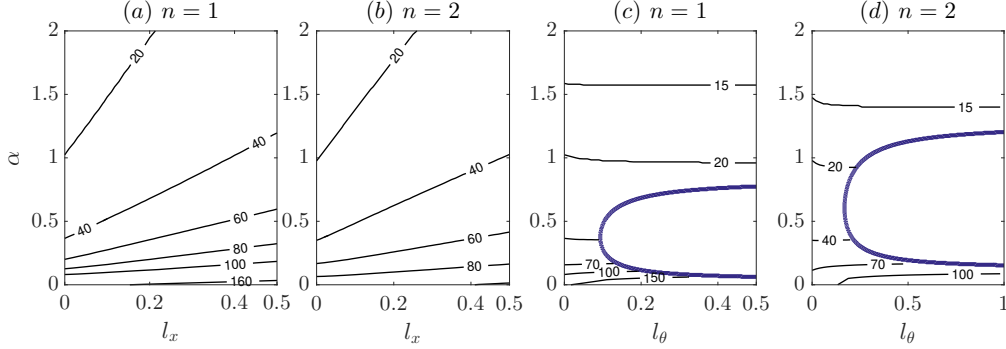


FIGURE 19. The time instant when G_{max} is reached, t_{max} , in the l_x - α plane for $n = 1$ (a) and $n = 2$ (b) and in the l_θ - α plane for $n = 1$ (c) and $n = 2$ (d).

Figure 18 shows G_{max} for the azimuthal slip case at $Re = 3000$ in the l_θ - α plane. Azimuthal wavenumbers $n = 1$ and $n = 2$ are considered. From the orientation of the contour lines we can see that azimuthal slip increases G_{max} . Presumably, azimuthal slip can enhance streamwise vortices because it reduces wall friction and allows finite azimuthal velocity at the wall, and therefore, the lift-up mechanism can be enhanced exhibiting increased transient growth as our results show. For $n = 1$, in the l_θ range investigated, the most amplified mode is still the $(\alpha, n) = (0, 1)$ mode as in the no-slip case. However, for $n = 2$, as l_θ increases, the most amplified mode is no longer the streamwise independent one but one with a small finite streamwise wavenumber (long wavelength), see panel (b). For example, the most amplified mode is approximately $\alpha = 0.05$ for l_θ above about 0.1. Similar behavior has also been reported for channel flow (Chai & Song 2019). The two bold lines in the figure enclose the linearly unstable regions in which G_{max} is theoretically infinite, therefore, the linearly unstable region is left blank. Unlike the streamwise slip case where the slip length significantly reduces the transient growth throughout the α and l_x ranges investigated (see Figure 17), azimuthal slip only significantly affects the transient growth for small α and nearly does not affect that of larger α , see the nearly horizontal contour lines for relatively large α . Besides, even for small α , G_{max} quickly saturates as l_θ increases. To sum up, azimuthal slip only affects the transient growth of the modes with small streamwise wavenumbers and the effect saturates as the slip length increases.

Figure 19 shows the time instant when G_{max} is reached, t_{max} , for the cases shown in Figure 17 and 18. In the streamwise slip case (panel (a,b)), for both $n = 1$ and 2, the slip increases t_{max} and the effect is more significant for larger α . In the azimuthal slip case (panel (c,d)), for small α ($\lesssim 0.2$), t_{max} is also slightly increased by the slip, whereas for larger α , t_{max} is slightly decreased by the slip, in contrast to the streamwise slip case. Overall, for the modes with small α , i.e. most amplified modes due to non-normality, both streamwise and azimuthal slip only mildly increase t_{max} .

In the no-slip case, the global G_{max} (maximized over α and n) is known to scale as Re^2 when Re is large (Meseguer & Trefethen 2003). In the presence of streamwise and azimuthal slip, the scaling is also investigated and shown in Figure 20. In the streamwise slip case (panel (a)), the lines for $l_x = 0.005, 0.05$ and 0.5 appear to be parallel to the no-slip case with a downward vertical shift, suggesting a Re^2 -scaling for any streamwise slip length. Similarly, for azimuthal slip, the scaling also seem to be Re^2 . For this case, we only investigated $l_\theta = 0.005$ and 0.02 in the linearly stable regime because larger l_θ will cause linear instability.

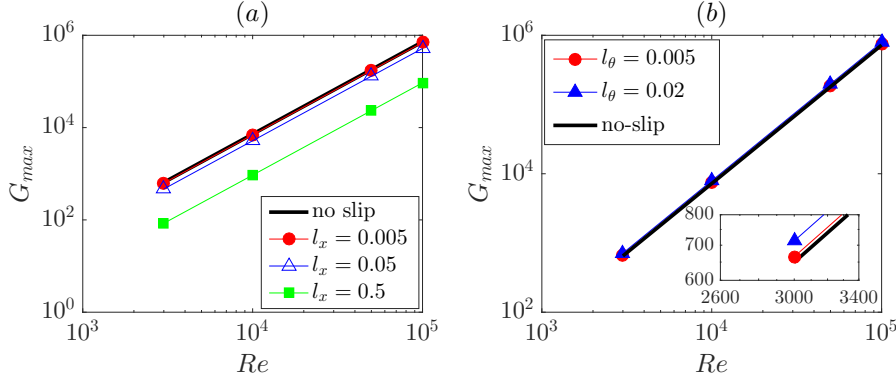


FIGURE 20. The scaling of global G_{max} with Re . (a) Streamwise slip $l_x = 0.005, 0.05$ and 0.5 . (b) Azimuthal slip $l_\theta = 0.005$ and 0.02 . In both panels, the bold black line shows the scaling for the no-slip case. The inset in (b) is a zoom-in around $Re = 3000$.

7. Conclusions and discussions

It has been well established that the classic pipe flow is (asymptotically) linearly stable. In this paper, we studied the effect of velocity slip on the linear stability of pipe flow. Our results show that the leading eigenvalue increases with streamwise slip length l_x but remains negative, i.e. streamwise slip renders the flow less stable but does not cause linear instability, similar to the effect of isotropic slip length on the flow (Průša 2009). Interestingly, our results suggest that the leading eigenvalue is independent of Re , or equivalently, the slowest decay rate of disturbances scales as Re^{-1} (note that time is scaled by Re^{-1} in our formulation). It should be pointed out that this scaling holds at sufficiently high Reynolds numbers ($\gtrsim 10^4$). For relatively low Reynolds numbers (100 and 1000 in our study), there is a very slight deviation from the scaling for $l_x \lesssim 0.1$ and the deviation is substantial at larger l_x . The Re^{-1} -scaling of the decay rate is the same as what was observed for the mode $(\alpha, n) = (0, 1)$ of the classic pipe flow by Meseguer & Trefethen (2003). Besides, our results show that the streamwise wavenumber at which the eigenvalue maximizes is not $\alpha = 0$ but also scales as Re^{-1} . However, if l_x is very large ($\gtrsim 1.0$, and note that in applications the slip length is generally much smaller), the eigenvalue maximizes at $\alpha = 0$ at relatively low Reynolds numbers (100 and 1000 in our study) and this scaling also only holds at high Reynolds numbers ($\gtrsim 10^4$).

This destabilizing effect appears to be opposite to the stabilizing effect of streamwise slip reported for channel flow (the stabilizing effect is mainly observed for 2-D perturbations) (Lauga & Cossu 2005; Min & Kim 2005; Chai & Song 2019). Here, we only provide a possible explanation for the least stable/most unstable perturbation (referred to as the leading perturbation for simplicity) of the two flows. We speculate that the different flow structures of the leading perturbations of the two flows are responsible. For pipe flow, we proved that the u_r component of the leading perturbation for $\alpha = 0$ modes vanishes. The globally leading perturbation has very small α ($\sim \frac{1}{Re}$), which indicates that u_r should be nearly vanishing. Therefore, the production rate of kinetic energy ($-\int_V u_r u_x \frac{dU_x}{dr} dV$) should be also very small and the decay rate of disturbances should be dominated by the dissipation rate. Intuitively, velocity slip reduces the dissipation rate due to the reduced wall friction, therefore, the decay rate of the least stable perturbation decreases, i.e. the flow appears to be destabilized. In contrast, for channel flow, the leading perturbations are 2-D Tollmien-Schlichting waves for small slip length, which have a substantial wall-normal velocity component (comparable to the streamwise

component). Therefore, the kinetic energy production is significant and even dominant in the variation of the kinetic energy. Streamwise slip reduces the base shear ($\frac{dU_x}{dr}$) and therefore subdues the production. If the reduction in the production rate outweighs the decrease in the energy dissipation rate due to the reduced wall friction, the flow will be stabilized. This is probably why stabilizing effect of the streamwise slip on channel flow was observed.

On the contrary, azimuthal slip, given sufficiently large slip length, causes linear instability, similar to the finding of Chai & Song (2019) for channel flow. Our results show that azimuthal slip destabilizes helical waves with wavelengths considerably larger than the pipe diameter, whereas it does not affect the stability of waves with much shorter wavelengths and in the long wavelength limit, i.e. $\alpha \rightarrow 0$. The critical Reynolds number decreases sharply as l_θ increases and gradually levels off at around a few hundred as $l_\theta \gtrsim 0.3$ and at approximately 260 as $l_\theta \rightarrow \infty$. Similar destabilizing effect was reported for channel flow (Chai & Song 2019). Azimuthal slip serves as an example for a perturbation to the linear operator associated with the linearized Navier-Stokes equations with no-slip boundary condition that destabilizes the originally stable system.

Regarding the stability of the classic pipe flow to streamwise independent perturbations, using an energy analysis, Joseph & Hung (1971) concluded the absolute and global stability of the flow, i.e. the flow is asymptotically (as $t \rightarrow \infty$) stable to such perturbations with arbitrary amplitude. Here, for the linear case and from a mathematical point of view, we rigorously proved that the eigenvalues of streamwise independent modes ($\alpha = 0$) are real and negative, for arbitrary slip length and arbitrary Reynolds number. Besides, the eigenvalue of the $\alpha = 0$ modes is proved to be strictly independent of Reynolds number in our formulation, in agreement with the numerical calculation by Meseguer & Trefethen (2003). We derived analytical solutions to the eigenvalue and eigenvector for $\alpha = 0$ modes and verified our theory by numerical calculations. We also proved that, the eigenvalues of $\alpha = 0$ modes consist of two groups: One group is associated with disturbances with $\Phi \equiv 0$, i.e. $u_r \equiv 0$, and the other is associated with disturbances with $\Phi \neq 0$, i.e. $u_r \neq 0$ (see Fig 13 and Figure 15). The two groups distribute alternately. For the streamwise slip case, the latter group stays constant while the former group changes with l_x . It is the other way round for the azimuthal slip case. Interestingly, for the streamwise slip case, the leading eigenvalue belongs to the $\Phi \equiv 0$ group and does not switch group as l_x changes, whereas for the azimuthal slip case, it switches from the $\Phi \equiv 0$ group to the $\Phi \neq 0$ group as l_θ crosses 1.0 from below (see Figure 15). When both l_x and l_θ are non-zero, l_x dominates the leading eigenvalue if $l_\theta < 1$. If $l_\theta > 1$, the leading eigenvalue first stays constant and can only start to increase at a threshold as l_x increases (see Figure 16). Such analytical solutions might inspire asymptotic analysis in the limit of small streamwise wavenumber.

Non-modal analysis shows that streamwise slip greatly reduces the transient growth, whereas azimuthal slip significantly increases the transient growth for disturbances with very small streamwise wavenumbers but nearly does not affect that for disturbances with larger streamwise wavenumbers, aside from the linear instability caused by the slip. Both streamwise slip and azimuthal slip give the Re^2 -scaling of the maximum transient growth, the same as in the no-slip case (Schmid & Henningson 1994; Meseguer & Trefethen 2003). Similar effects were observed for channel flow (Chai & Song 2019).

Linear instability caused by anisotropic slip at low Reynolds numbers is of interest for small flow systems, such as microfluidics, in which the Reynolds number is usually low but the non-dimensional slip length can be significantly large using advanced surface texturing techniques. The instability can be exploited to enhance mixing or heat transfer in applications involving small flow systems. Larger non-modal growth caused by azimuthal

slip can potentially cause earlier subcritical transition to turbulence. Besides, introducing modal instability into originally sub-critical flows may also help to better understand the transition mechanism in such flows.

8. Acknowledgements

The authors acknowledge financial support from the National Natural Science Foundation of China under grant number 91852105 and 91752113 and from Tianjin University under grant number 2018XRX-0027. The comments from the reviewers are also highly appreciated.

9. Declaration of interests

The authors report no conflict of interest.

Appendix A. Numerics

Firstly, we briefly explain the implementation of the boundary condition (2.10) and (2.11) in the eigenvalue problem for the linear system (2.2).

The eigenvalue equation reads

$$-L^{-1}M\mathbf{q} = \lambda\mathbf{q}, \quad (\text{A } 1)$$

where \mathbf{q} is the unknown vector composed of $\hat{\Phi}$ and $\hat{\Omega}$, see (2.5). Boundary conditions (2.10) and (2.11) couple $\hat{\Phi}$ and $\hat{\Omega}$, unlike in the no-slip case. In our Fourier-Fourier-Chebyshev collocation discretization, \mathbf{q} is a $2N \times 1$ vector and the operator $-L^{-1}M$ is discretized as a $2N \times 2N$ matrix, where N is the number of collocation grid point on the radius. Adopting the Chebyshev differentiation matrix of Trefethen (2000) which is of spectral accuracy, the matrix is dense and the radial differentiation of \mathbf{q} at a single grid point is calculated using the value of \mathbf{q} at all collocation points on the radius. Given that $\hat{\Phi}$ is known at $r = 1$, i.e. $\hat{\Phi} = 0$ at $r = 1$, the size of the system can be reduced by one. The boundary conditions (2.10) and (2.11) give two linear algebraic equations about $\hat{\Phi}$ and $\hat{\Omega}$ at the collocation points, from which we can further eliminate two unknowns. By doing so, the system size is reduced by 3, i.e. to $(2N - 3) \times (2N - 3)$, from which the eigenvalue problem can be solved with the boundary conditions being taken accounted for.

Secondly, we show the convergence test of our numerical calculation. We consider the case of $Re = 3000$, $\alpha = 0.5$ and $n = 1$, as presented in Figure 1(b) and Figure 6(b). We change the number of Chebyshev points and check the convergence of the mean-mode, wall-mode and center-mode separately. Table 1, 2 and 3 shows the resolutions and the eigenvalue of an arbitrarily selected mean mode and the rightmost eigenvalues corresponding to the wall- and center-mode. It can be seen that grid numbers $N = 32$, 64 and 128 give very close values of the eigenvalues, which differ only after about 7 digits after the decimal point (the relative difference is $\mathcal{O}(10^{-11})$), for all the slip length of 0.005, 0.05, 0.5 and the case of $l_\theta = \infty$. The convergence test show that, for the calculation of the rightmost eigenvalues and for calculating the mean mode at $Re = 3000$, 32 points are sufficient. Solely for calculating the rightmost eigenvalue, we used 32 points for $Re = 100$, 1000 and 10000, and 64 points for $Re = 10^5$ and $Re = 10^6$. We checked the convergence by doubling the number of grid points and found these numbers sufficient. It should be noted that, although 32 points are sufficient for calculating both of the rightmost eigenvalue and the spectrum at $Re = 3000$, more grid points may be needed for accurately calculating

$Re = 3000, \alpha = 0.5, n = 1, l_x = 0.005 \text{ and } l_\theta = 0$		
N	mean-mode	wall-mode
32	-622.180970763082-1006.803438258427 <i>i</i>	-106.901701568167-600.000309196652 <i>i</i>
64	-622.180970617437-1006.803438460110 <i>i</i>	-106.901701568129-600.000309195248 <i>i</i>
128	-622.180970549502-1006.803438403115 <i>i</i>	-106.901701574121-600.000309193566 <i>i</i>
N	center-mode	
32	-87.144443682906-1299.140360156589 <i>i</i>	
64	-87.144443682943-1299.140360156482 <i>i</i>	
128	-87.144443681739-1299.140360155874 <i>i</i>	

$Re = 3000, \alpha = 0.5, n = 1, l_x = 0.05 \text{ and } l_\theta = 0$		
N	mean-mode	wall-mode
32	-530.922788817816-953.518793751342 <i>i</i>	-68.522846170133-646.557599422173 <i>i</i>
64	-530.922788815748-953.518793737632 <i>i</i>	-68.522846166147-646.557599425783 <i>i</i>
128	-530.922788808102-953.518793754673 <i>i</i>	-68.522846166147-646.557599425783 <i>i</i>
N	center-mode	
32	-80.309678415026-1203.366029301252 <i>i</i>	
64	-80.309678415070-1203.366029301237 <i>i</i>	
128	-80.309678413737-1203.366029300673 <i>i</i>	

$Re = 3000, \alpha = 0.5, n = 1, l_x = 0.5 \text{ and } l_\theta = 0$		
N	mean-mode	wall-mode
32	-582.2041335894776-833.8681859837275 <i>i</i>	-32.3669400581618-546.6565442837639 <i>i</i>
64	-582.2041335893674-833.8681859850334 <i>i</i>	-32.3669400570418-546.6565442835596 <i>i</i>
128	-582.2041336044291-833.8681859835294 <i>i</i>	-32.3669400643051-546.6565442852506 <i>i</i>
N	center-mode	
32	-36.8382964038017-757.7599724649968 <i>i</i>	
64	-36.8382964035955-757.7599724652722 <i>i</i>	
128	-36.8382963977050-757.7599724664044 <i>i</i>	

TABLE 1. The convergence of the eigenvalue corresponding to the mean mode (arbitrarily selected) and the rightmost wall-mode and center-mode as the radial grid number N . The stream-wise slip cases of $l_x = 0.005, 0.05$ and 0.5 for $Re = 3000, \alpha = 0.5, n = 1$ and $l_\theta = 0$ are listed.

the spectrum than for calculating the rightmost eigenvalue at higher Reynolds numbers (Trefethen 2000; Meseguer & Trefethen 2003).

Appendix B. The dependence of the leading eigenvalue on the azimuthal wavenumber n for $\alpha = 0$

Our numerical calculations in Section 3 and 4 showed that $n = 1$ modes are the least stable/most unstable modes. Here we show the dependence of $\max \lambda$ of $\alpha = 0$ modes on the azimuthal wavenumber n and prove that $n = 1$ is indeed the least stable azimuthal

$Re = 3000, \alpha = 0.5, n = 1, l_\theta = 0.005 \text{ and } l_x = 0$		
N	mean-mode	wall-mode
32	-878.143428857252-1000.225260064803 <i>i</i>	-147.212095816072-565.187041064729 <i>i</i>
64	-878.143429638119-1000.225258436485 <i>i</i>	-147.212095816866-565.187041057138 <i>i</i>
128	-878.143429646590-1000.225258451813 <i>i</i>	-147.212095817673-565.187041057973 <i>i</i>

N	center-mode
32	-88.016026669448-1311.995868654545 <i>i</i>
64	-88.016026669520-1311.995868654469 <i>i</i>
128	-88.016026668333-1311.995868653794 <i>i</i>

$Re = 3000, \alpha = 0.5, n = 1, l_\theta = 0.05 \text{ and } l_x = 0$		
N	mean-mode	wall-mode
32	-818.018362966476-992.813175584590 <i>i</i>	-30.701258513947-434.347551571943 <i>i</i>
64	-818.018361688704-992.813172416195 <i>i</i>	-30.701258511491-434.347551570607 <i>i</i>
128	-818.018361708603-992.813172372158 <i>i</i>	-30.701258513706-434.347551572422 <i>i</i>

N	center-mode
32	-88.015855528115-1312.001178576785 <i>i</i>
64	-88.015855528186-1312.001178576701 <i>i</i>
128	-88.015855526922-1312.001178575825 <i>i</i>

$Re = 3000, \alpha = 0.5, n = 1, l_\theta = 0.5 \text{ and } l_x = 0$		
N	mean-mode	wall-mode
32	-794.161410360041-1006.311883474201 <i>i</i>	33.866513836957-391.619593748286 <i>i</i>
64	-794.161408826090-1006.311880389063 <i>i</i>	33.866513839707-391.619593747032 <i>i</i>
128	-794.161408715927-1006.311880293383 <i>i</i>	33.866513840046-391.619593749138 <i>i</i>

N	center-mode
32	-88.013747237500-1312.003625793072 <i>i</i>
64	-88.013747237549-1312.003625792987 <i>i</i>
128	-88.013747236338-1312.003625792171 <i>i</i>

TABLE 2. The convergence of the eigenvalue corresponding to the mean mode (arbitrarily selected) and the rightmost wall-mode and center-mode as the radial grid number N . The azimuthal slip cases of $l_\theta = 0.005, 0.05$ and 0.5 for $Re = 3000, \alpha = 0.5, n = 1$ and $l_x = 0$ are listed.

mode. For this purpose, we only need to prove that the minimum non-zero roots of Eqs. (5.43) and (5.47) all increase with n .

Note that the root of Eqs. (5.43) is independent of l_x . Because the zeros of $J_n(z)$ and $J_{n+1}(z)$ distribute alternately, it can be easily seen that, if $l_\theta \leq 1$, the minimum positive root of Eqs. (5.43) is located between the minimum positive zeros of $J_n(z)$ and $J_{n+1}(z)$. Therefore, the minimum positive root of Eqs. (5.43) increases with n because the positive zeros of $J_n(z)$ and $J_{n+1}(z)$ all increase with n , i.e., λ_1 decreases as n increases if $l_\theta \leq 1$.

If $l_\theta > 1$, we need to prove that the minimum positive root of

$$g_n(z) = (1 - l_\theta)J_n(z) + l_\theta z J_{n-1}(z) = 0, \quad n \geq 2 \quad (\text{B } 1)$$

$Re = 3000, \alpha = 0.5, n = 1, l_\theta = \infty$ and $l_x = 0$		
N	mean-mode	wall-mode
32	-637.771735030362-1019.911762553870i	45.558397965700-383.081240915272i
64	-637.771735090255-1019.911762536828i	45.558397968779-383.081240913500i
128	-637.771735157437-1019.911762419706i	45.558397965363-383.081240919212i

N	center-mode
32	-88.013312066798-1312.003902287461i
64	-88.013312066887-1312.003902287400i
128	-88.013312039270-1312.003902226469i

TABLE 3. The convergence of the eigenvalue corresponding to the mean mode (arbitrarily selected) and the rightmost wall-mode and center-mode as the radial grid number N . The azimuthal slip case of $l_\theta = \infty$ for $Re = 3000, \alpha = 0.5, n = 1$ and $l_x = 0$ is listed.

is smaller than that of $g_{n+1}(z) = 0$, i.e. Eqs. (5.43). We already showed in Eqs. (5.51) that $F(z, l_\theta) > 0$ at sufficiently small z , i.e. $g_n(z) > 0$ for sufficiently small z . Denoting the minimum positive root of Eqs. (5.43) as z_0 , we only need to show that $g_n(z_0) < 0$. Using the property of Bessel function of

$$J_{n+1}(z) + J_{n-1}(z) = \frac{2n}{z} J_n(z) \quad (\text{B } 2)$$

and Eqs. (5.43), $g_n(z)$ can be rewritten as

$$g_n(z_0) = (1 - l_\theta) J_n(z_0) + l_\theta z_0 \left(\frac{2n}{z_0} - \frac{l_\theta}{l_\theta - 1} z_0 \right) J_n(z_0). \quad (\text{B } 3)$$

It is easily seen that $J_n(z_0) > 0$, therefore, we need to show that

$$(1 - l_\theta) + l_\theta z_0 \left(\frac{2n}{z_0} - \frac{l_\theta}{l_\theta - 1} z_0 \right) < 0, \quad (\text{B } 4)$$

or equivalently,

$$z_0^2 > (1 - l_\theta^{-1})(2n - 1 + l_\theta^{-1}), \quad (\text{B } 5)$$

in order to prove that $g_n(z_0) < 0$, given $l_\theta > 1$. Noticing that $(1 - l_\theta^{-1})(2n - 1 + l_\theta^{-1}) < 2n - 1$ if $l_\theta > 1$, we can prove $g_n(z_0) < 0$ if we can show that $z_0^2 > 2n - 1$.

In Section 5.3 we proved that the minimum positive root of Eqs. (5.43) decreases as l_θ increases, therefore, z_0 is minimized at $l_\theta = +\infty$. To prove that $z_0^2 > 2n - 1$ for any $l_\theta > 1$, we only need to show that $z_0^2 > 2n - 1$ holds for $l_\theta = +\infty$, with which Eqs. (5.43) reduces to $J_{n+1}(z) - z J_n(z) = 0$. That $F(z, l_\theta) > 0$ at sufficiently small z indicates that $J_{n+1}(z) - z J_n(z) < 0$ at sufficiently small z given $l_\theta = +\infty$. Therefore, $J_{n+1}(z_0) - z_0 J_n(z_0) = 0$ requires that $J_{n+1}(z) - z J_n(z) < 0$, i.e. $J_{n+1}(z) < z J_n(z)$ for any $z < z_0$. In fact, we can show that $J_{n+1}(z) < z J_n(z)$ if $0 < z^2 < 2n - 1$ such that z_0 has to satisfy $z_0^2 > 2n - 1$. Using the series form of Bessel function, $J_{n+1}(z) < z J_n(z)$ means

$$\sum_{k=0}^{+\infty} \frac{(-1)^2}{k!} \frac{1}{(n+k+1)!} \left(\frac{z}{2} \right)^{2k+n+1} < z \sum_{k=0}^{+\infty} \frac{(-1)^2}{k!} \frac{1}{(n+k)!} \left(\frac{z}{2} \right)^{2k+n}. \quad (\text{B } 6)$$

Because of the absolute convergence of the two infinite series in Eqs. (B 6), we only need

to show that for any positive even number k ,

$$\frac{1}{k!} \frac{1}{(n+k+1)!} \left(\frac{z}{2}\right)^{2k+n+1} - \frac{1}{(k+1)!} \frac{1}{(n+k+2)!} \left(\frac{z}{2}\right)^{2k+2+n+1} < \frac{z}{k!} \frac{1}{(n+k)!} \left(\frac{z}{2}\right)^{2k+n} - \frac{z}{(k+1)!} \frac{1}{(n+k+1)!} \left(\frac{z}{2}\right)^{2k+2+n}, \quad (\text{B } 7)$$

if $0 < z^2 < 2n - 1$. Rearranging Eqs. (B 7), we have

$$z^2 < 4(k+1)(n+k+2), \quad (\text{B } 8)$$

which obviously holds because $z^2 < 2n - 1 < 4n + 4k + 8 \leq 4(k+1)(n+k+2)$. To sum up, we have proved that $J_{n+1}(z) < zJ_n(z)$ if $z^2 < 2n - 1$, therefore, z_0 , which satisfies $J_{n+1}(z_0) - z_0 J_n(z_0) = 0$, must satisfy $z_0^2 > 2n - 1$. Consequently, Eqs. (B 5) and $g_n(z_0) < 0$ hold, and thusly the minimum positive root of Eqs. (B 1) is smaller than z_0 , which indicates that the minimum positive root of Eqs. (5.43) increases with n , i.e. λ_1 decreases with n .

Next, we prove that the minimum positive root of Eqs. (5.47) also increases with n . The equation

$$h_n(z) = (1 + nl_x)z^n J_n(z) - l_x z^{n+1} J_{n+1}(z) = 0 \quad (\text{B } 9)$$

share the non-zero roots with Eqs. (5.47), therefore, we only need to prove the same statement for Eqs. (B 9). Denoting the minimum positive zero of $h_{n-1}(z)$ as z_0 , we next show that $h_n(z)$ monotonically increases in $[0, z_0]$ such that there is no positive root of Eqs. (B 9) in $[0, z_0]$, i.e. the minimum positive root of Eqs. (B 9) increases with n . Using the property of Bessel function of $(z^{n+1} J_{n+1}(z))' = z^{n+1} J_n(z)$, where $'$ denotes the derivative with respect to z , we take the derivative of $h_n(z)$ with respect to z and obtain

$$h'_n(z) = (1 + nl_x)z^n J_{n-1}(z) - l_x z^{n+1} J_n(z) = z(h_{n-1}(z) + l_x z^{n-1} J_{n-1}(z)). \quad (\text{B } 10)$$

It is easy to see that $h_{n-1}(z)$ is positive at sufficiently small z (the derivation is similar to that of $F(z, l_\theta)$ being positive at sufficiently small z , see Eqs. (5.51)), consequently, $h_{n-1}(z) > 0$ in $(0, z_0)$. As z_0 is smaller than the minimum positive zero of $J_{n-1}(z)$, we have $J_{n-1}(z) > 0$ in $(0, z_0)$. Therefore, $h'_n(z) > 0$ in $(0, z_0)$, i.e. $h_n(z)$ monotonically increases and there is no positive root of Eqs. (B 9) in $(0, z_0]$. In other words, the minimum positive root of $h_n(z) = 0$ is always larger than that of $h_{n-1}(z) = 0$, i.e. the minimum positive root of Eqs. (5.47) increases with n , and therefore λ_2 decreases with n . Now, we reach the conclusion that $\max \lambda = \max\{\lambda_1, \lambda_2\}$ decreases with n for $\alpha = 0$ modes because λ_1 and λ_2 both decrease with n .

REFERENCES

- ASMOLOV, E. S. & VINOGRADOVA, O. I. 2012 Effective slip boundary conditions for arbitrary one-dimensional surfaces. *J. Fluid Mech.* **706**, 108–117.
- AVILA, K., MOXEY, D., DE LOZAR, A., AVILA, M., BARKLEY, D. & HOF, B. 2011 The onset of turbulence in pipe flow. *Science* **333**, 192–196.
- BAZANT, M. Z. & VINOGRADOVA, O. I. 2008 Tensorial hydrodynamic slip. *J. Fluid Mech.* **613**, 125–134.
- BELYAEV, A. V. & VINOGRADOVA, O. I. 2010 Effective slip in pressure-driven flow past super-hydrophobic stripes. *J. Fluid Mech.* **652**, 489–499.
- BRANDT, L. 2014 The lift-up effect: the linear mechanism behind transition and turbulence in shear flows. *Eur. J. Mech. B/Fluids* **47**, 80–96.
- CHAI, C. & SONG, B. 2019 Stability of slip channel flow revisited. *Phys. Fluids* **31**, 084105.

- CHATTOPADHYAY, G., USHA, R. & SAHU, K. C. 2017 Core-annular miscible two-fluid flow in a slippery pipe: A stability analysis. *Phys. Fluids* **29**, 097106.
- CHEN, Q., WEI, D. & ZHANG, Z. 2019 Linear stability of pipe Poiseuille flow at high Reynolds number regime. *arXiv:1910.14245v1 [math.AP]*.
- DRAZIN, P. G. A. & REID, W. H. 1981 *Hydrodynamic Stability*. Cambridge University Press.
- ECKHARDT, B., SCHNEIDER, T. M., HOF, B. & WESTERWEEL, J. 2007 Turbulence transition in pipe flow. *Annu. Rev. Fluid Mech.* **39**, 447–68.
- GAN, C.-J. & WU, Z.-N. 2006 Short-wave instability due to wall slip and numerical observation of wall-slip instability for microchannel flows. *J. Fluid Mech.* **550**, 289–306.
- GHOSH, S., USHA, R. & SAHU, K. C. 2014 Linear stability analysis of miscible two-fluid flow in a channel with velocity slip at the walls. *Phys. Fluids* **26**, 014107.
- HERRON, I. H. 1991 Observations on the role of vorticity in the stability theory of wall bounded flows. *STUDIES IN APPLIED MATHEMATICS* **85**, 269–286.
- HERRON, I. H. 2017 A unified solution of several classical hydrodynamic stability problems. *QUARTERLY OF APPLIED MATHEMATICS* **LXXXVI**, 1–17.
- HU, H. H. & JOSEPH, D. D. 1989 Lubricated pipelining : stability of core-annular flow. part 2. *J. Fluid Mech.* **205**, 359–396.
- JOSEPH, D. D. 1997 Core-annular flows. *Annu. Rev. Fluid Mech.* **29**, 65–90.
- JOSEPH, D. D. & HUNG, W. 1971 Contributions to the nonlinear theory of stability of viscous flow in pipes and between rotating cylinders. *Arch. Rational Mech. Anal.* **44**, 1–22.
- LAUGA, E. & COSSU, C. 2005 A note on the stability of slip channel flows. *Phys. Fluids* **17**, 088106.
- LECOQ, N., ANTHORE, R., CICHOCKI, B., SZYMCAK, P. & FEUILLEBOIS, F. 2004 Drag force on a sphere moving towards a corrugated wall. *J. Fluid Mech.* **513**, 247–264.
- LEE, C., CHOI, C.-H. & JIM, C.-J 2008 Structured surfaces for a giant liquid slip. *Phys. Rev. Lett.* **101**, 064501.
- LEE, C. & JIM, C.-J 2009 Maximizing the giant liquid slip on superhydrophobic microstructures by nanostructuring their sidewalls. *Langmuir* **25**, 12812.
- LI, JIE & RENARDY, YURIKO 1999 Direct simulation of unsteady axisymmetric core-annular flow with high viscosity ratio. *J. Fluid Mech.* **391**, 123–149.
- MESEGUER, A. & TREFETHEN, L.N. 2003 Linearized pipe flow to Reynolds number 10^7 . *J. Comput. Phys.* **186**, 178–197.
- MIN, T. & KIM, J. 2005 Effects of hydrophobic surface on stability and transition. *Phys. Fluids* **17**, 108106.
- NG, C.-O. & WANG, C. Y. 2009 Stokes shear flow over a grating: Implications for superhydrophobic slip. *Phys. Fluids* **21**, 013602.
- PRALITS, J. O., ALINOV, E. & BOTTARO, A. 2017 Stability of the flow in a plane microchannel with one or two superhydrophobic walls. *PHYSICAL REVIEW FLUIDS* **2**, 013901.
- PRŮŠA, V. 2009 On the influence of boundary condition on stability of Hagen-Poiseuille flow. *Computers and Mathematics with Applications* **57**, 763–771.
- REN, L., CHEN, J.-G. & ZHU, K.-Q. 2008 Dile role of wall slip on linear stability of plane Poiseuille flow. *Chin. Phys. Lett.* **26**, 601–603.
- ROTHSTEIN, J. P. 2010 Slip on superhydrophobic surfaces. *Annu. Rev. Fluid Mech.* **42**, 89–109.
- SAHU, K. C. 2016 Double-diffusive instability in core-annular pipe flow. *J. Fluid Mech.* **789**, 830–855.
- SCHMID, P. J 2007 Nonmodal stability theory. *Ann. Rev. Fluid Mech.* **39**, 129–162.
- SCHMID, P. J & HENNINGSON, D. S. 1994 Optimal energy density growth in hagen-poiseuille flow. *J. Fluid Mech.* **277**, 197–225.
- SELVAM, B., MERK, S., GOVINDARAJAN, R. & MEIBURG, E. 2007 Stability of miscible core-annular flows with viscosity stratification. *J. Fluid Mech.* **592**, 23–49.
- SEO, J. & MANI, A. 2016 On the scaling of the slip velocity in turbulent flows over superhydrophobic surfaces. *Phys. Fluids* **28**, 025110.
- SQUIRE, H. B. 1933 On the stability of three dimensional disturbances of viscous flow between parallel walls. *Proc. Roy. Soc. A* **142**, 621–638.
- TREFETHEN, L. N. 2000 *Spectral methods in Matlab*. SIAM.

- VINOGRADOVA, O. I. 1999 Slippage of water over hydrophobic surfaces. *Int. J. Min. Process* **56**, 31–60.
- VORONOV, R. S., PAPAVALASSIOU, D. V. & LEE, L. L. 2008 Review of fluid slip over superhydrophobic surfaces and its dependence on the contact angle. *Industr. Eng. Chem. Res.* **47**, 2455–2477.